TECHNICAL UNIVERSITY OF CRETE

THESIS

EEG Source Localization on Different Realistic Brain Anatomies using Deep Learning Techniques

Author:
Afroditi Kolomvaki

Supervisor:
Prof. Michalis Zervakis

A thesis submitted in fulfillment of the requirements for the degree in Electrical and Computer Engineering

in the

Digital Image and Signal Processing Laboratory
Department of Electrical & Computer Engineering

June 11, 2024

Thesis Committee

Prof. Michalis Zervakis (Supervisor)
Prof. Athanasios Liavas
Prof. Carsten Wolters

TECHNICAL UNIVERSITY OF CRETE

Abstract

Department of Electrical & Computer Engineering

Electrical and Computer Engineering

EEG Source Localization on Different Realistic Brain Anatomies using Deep Learning Techniques

by Afroditi Kolomvaki

Electroencephalography (EEG) is a technique used to record the electrical activity of the brain and is commonly used in medical settings to diagnose and monitor conditions such as epilepsy, sleep disorders, and brain injuries. It involves placing electrodes on the scalp, which detect the electrical signals produced by the brain. One of the main challenges in interpreting these EEG signals is to identify the underlying neural sources responsible for generating the measured scalp potentials. This is known as EEG source analysis or EEG inverse problem. Various numerical methods exist to address this inverse problem, but they require considerable computational time and often depend heavily on prior assumptions. Recently, neural networks have been suggested as a solution, but their training often relies on suboptimal forward modeling and they struggle to localize EEG signals across different brain anatomies and multiple brain electrical activations. In this study, we introduce a Convolutional Neural Network (CNN) architecture that is independent of the brain source space model and trained using realistic head models calibrated for skull conductivity. It is capable of solving the inverse problem for up to three active brain sources on different realistic brain anatomies. The results indicate that our CNN outperforms traditional numerical methods like sLORETA.

Acknowledgements

I would like to thank my supervisor, Prof. Michalis Zervakis, as well as Dr. Marios Antonakakis, for exposing me to this fascinating research area and for their guidance and support. I would also like to thank the members of my thesis committee, Prof. Athanasios Liavas and Prof. Carsten Wolters for making my defense an enjoyable moment and for their brilliant comments. I extend my sincere thanks to Prof. Michail Lagoudakis and Prof. George Karystinos for their help and support during my graduate school applications. Last but not least, I am grateful to my close friends and family, who were also an important part of my journey during my studies at the Technical University of Crete.

Contents

List of Figures

List of Tables

Chapter 1

Introduction

1.1 Motivation

Brain source analysis is a technique used in neuroscience to identify and localize the neural sources of various signals measured on the scalp, such as electroencephalography (EEG), magnetoencephalography (MEG), or electrocorticography (ECoG) [1].

EEG (electroencephalography) is a non-invasive technique that measures the electrical activity of the brain by placing electrodes on the scalp. It is a valuable tool for studying brain function, diagnosing neurological disorders, and monitoring brain activity. One of the main challenges in interpreting EEG signals is to identify the underlying neural sources responsible for generating the measured scalp potentials. This is known as EEG source analysis or EEG inverse problem. It's worth noting that the inverse problem in brain source analysis is closely related to the forward problem. In fact, solving the inverse problem requires the solution of the forward problem, which aims to predict the scalp measurements based on known or estimated neural sources, as opposed to the inverse problem that seeks to estimate the neural activity inside the brain given the measured scalp data.

By estimating the neural sources responsible for the measured signals, researchers can infer the spatial distribution of neural activity within the brain. This information is valuable for understanding brain function, studying cognitive processes, and investigating neurological disorders. For example, EEG source analysis enables the localization of abnormal brain activity in patients with epilepsy, tumors, or other neurological disorders, which can guide surgical planning and treatment [2].

As Deep Learning is considered to be a promising new approach for solving the inverse problem [3, 4, 5, 6], this thesis presents a new Convolutional Neural Network that performs source localization for up to three sources and for different realistic brain anatomies in real time. The first step for solving this problem is to create a realistic computational model of the head and its various tissues to accurately simulate and localize the sources of electrical signals recorded from the scalp using electroencephalography (EEG). In this thesis, the source space, which is a set of all candidate dipole[1] positions in the brain, consists of 50,460 dipoles and a set of 74 electrodes, while also following the 10-10 system configuration and a level of precision at the millimeter scale. An accurate head volume conductor model is also crucial for capturing both the geometric and dielectric characteristics of the head. Precise estimation of these properties is essential for obtaining reliable solutions in both forward and inverse analyses. However, achieving this accuracy is challenging due to the presence of numerous head tissues with varying conductivities and the differences in conductivity observed among individuals. Notably, the human skull's

[1] A dipole is a source point inside the brain that generates electrical activity

conductivity is particularly variable and requires careful consideration in the modeling process [7]. In this tesis, a six-compartment head model (6C) has been utilized, which consists of:

- skin
- skull compacta
- Cerebrospinal fluid (CSF)
- skull spongiosa
- grey matter
- white matter

The robustness of the model is tested with both simulated and real data, using a higher noise levels than the one that was used for the training process. The architecture was inspired by other commonly used deep learning models, like AlexNet [8] and VGG [9] and the final choice for the CNN was based upon experimenting and measuring the error in source localization during the validation process. We also experiment with a ResNet [10] architecture.

Our results suggest that our model is able to accurately localize EEG recordings to three different anatomies and with up to three dipoles in the brain for various SNR levels. Even though all the numerical methods can also localize EEG to different brain anatomies, they require the leadfield matrix of each subject (i.e. the solution of the forward problem). Since, the solution of the forward problem needs approximately 40 minutes, numerical methods cannot provide real-time EEG source localization. Due to the fact that our CNN does not need the leadfield matrix of each subject (once trained), it can provide real-time source localization for various anatomies.

1.2 Related Work

The first pioneer studies that proposed an artificial neural network as a solution to the inverse problem are [11, 12, 13]. However, these studies are limited by the sample size, network depth and computational power at that time, leading to a poor performance. In recent years, several deep learning methods have been proposed for the inverse problem. Among them, two Multi-Layer Perceptron(MLP) networks [4, 6] and various CNNs such as [3, 14, 15]. The aforementioned neural network-based inverse solutions are based on suboptimal forward modeling and they cannot localize EEG recordings in various brain anatomies. However, they have been tested in a distributed dipole model with more than two dipole sources. The most closely related work to ours is feCNN [5] where they also solve the Forward Problem with FEM [16] and with the same head-model [7]. However, our method has three key differences with feCNN:

1. feCNN can localize EEG recordings to only one dipole in the brain, while our model has the ability to localize up to three dipoles.
2. Our model is trained with simulated data from three brain anatomies, while feCNN is trained with simulated data from only one.
3. feCNN utilizes FSL Registration [17, 18, 19] to localize EEG recordings to various brain anatomies while our model directly localizes to different brain anatomies

Studying numerical algorithms for solving the EEG inverse problem has a rich history, with these methods typically falling into three categories: non-parametric methods [20], parametric methods [20], and Bayesian methods [21]. Among non-parametric solutions, one of the most renowned approaches is minimal norm estimation (MNE) [22]. As indicated by [23], MNE excels in cases where limited prior knowledge about the source distribution is available. In addition to MNE, low-resolution electromagnetic tomography (LORETA) [24] offers effective 3D localization compared to previous minimum norm methods. A variant of LORETA, standardized LORETA (sLORETA) [25], leverages MNE to estimate current density and further standardizes it using expected standard deviation. Another LORETA variation is exact LORETA (eLORETA) [26], which places greater emphasis on deeper sources. Another promising inverse method is beamforming, which involves applying spatial filtering to recorded data to discriminate signals originating from a specific region of interest while suppressing those from other sources [7].

Even though, these methods are verified to many studies [20, 27], they still have limitations. In particular, although MNE offers good results in terms of resolution and current estimation, it is unable to address the issue of deep source localization in the outermost cortex [28]. In addition, unlike the MNE solution, LORETA can localize the boundary and deep sources. However, the solution provided has low spatial resolution, which is an undesirable feature when we are dealing with pattern-recognition applications of brain source localization [28]. Furthermore, localization accuracy of sLORETA and eLORETA methods is better than LORETA, but their spatial resolution is not appropriate [27]. Finally, drawbacks of the beamforming approach are the susceptibility to imprecisions in the forward model and that correlated sources are often not found [3].

Chapter 2

Brain Anatomy and EEG

2.1 The Human Brain

The brain is a complex and vital organ that serves as the central command center of the nervous system. It is responsible for controlling and coordinating various bodily functions, as well as enabling perception, cognition, memory, emotions, and behavior.

The brain is primarily made up of two types of tissue: gray matter and white matter.

- Gray Matter: Gray matter is composed of neuron cell bodies, dendrites, and glial cells. It forms the outer layer of the cerebrum and is also found in clusters called nuclei deep within the brain. Gray matter is responsible for processing information, decision-making, and controlling voluntary movements.
- White Matter: White matter consists of bundles of myelinated nerve fibers called axons. These axons connect different regions of the brain, allowing for communication and the transmission of signals between neurons. The myelin sheath, which surrounds the axons, gives white matter its white appearance. White matter helps in the coordination and integration of various brain functions.

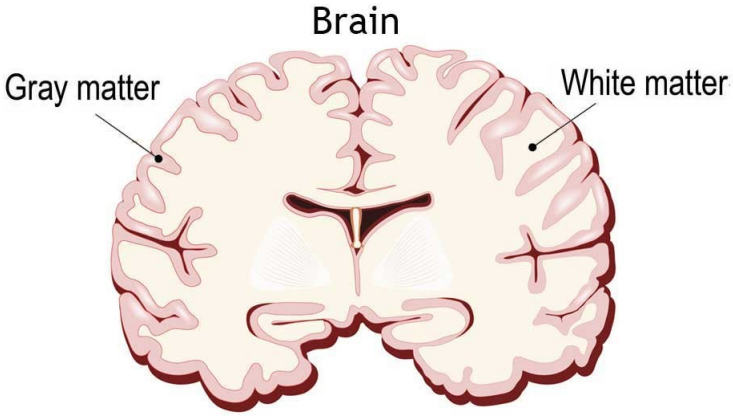

FIGURE 2.1: Grey and White matter in the brain

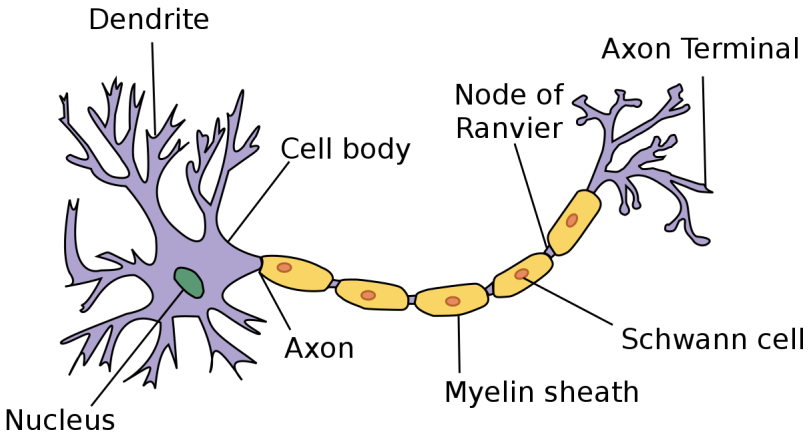

FIGURE 2.2: Basic neuron structure

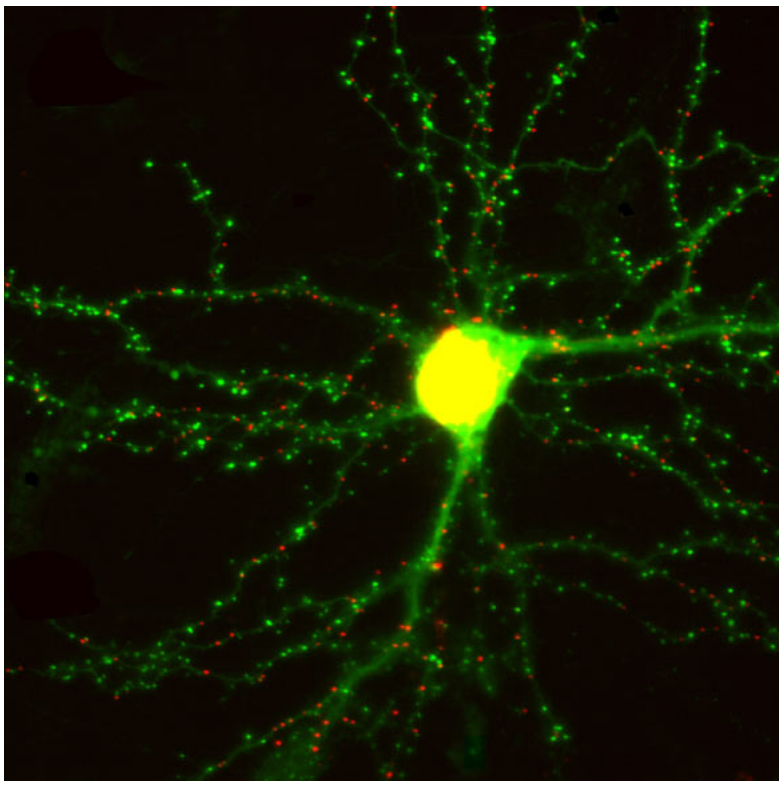

FIGURE 2.3: This image shows a living neuron in culture: green dots indicate excitatory synapses; red dots indicate inhibitory synapse. [29]

s

2.2 Main Parts of the Brain and Their Functions

At a high level, the brain can be divided into the Cerebrum, Brainstem and Cerebellum.

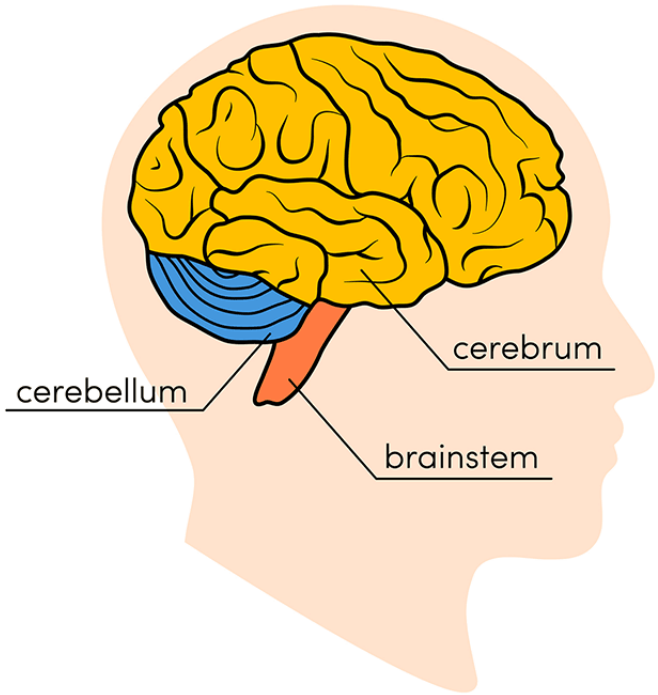

FIGURE 2.4: The three main parts of the brain

- The **Cerebrum**, situated at the front of the brain, consists of two primary components: the cerebral cortex, which is composed of gray matter, and the white matter located at its core. As the largest portion of the brain, the cerebrum plays a central role in initiating and coordinating movements, as well as regulating body temperature. Moreover, various regions within the cerebrum facilitate essential functions such as speech, judgment, thinking, reasoning, problem-solving, emotions, and learning. Additionally, specific areas of the cerebrum are dedicated to processing visual, auditory, tactile, and other sensory information.

  Cerebral Cortex

  The term "cortex" originates from the Latin word "bark" and refers to the outer layer of gray matter that covers the cerebrum. This cortex possesses a substantial surface area due to its folds and constitutes approximately half of the brain's overall weight. The cerebral cortex is divided into two hemispheres and exhibits a textured appearance with ridges (gyri) and folds (sulci). These two hemispheres are connected by a prominent and deep sulcus known as the interhemispheric fissure, also referred to as the medial longitudinal fissure. This fissure extends from the front to the back of the head. Notably, the right hemisphere of the brain governs the left side of the body, while the left hemisphere controls the right side. Communication between the two hemispheres is facilitated by a large, C-shaped structure consisting of white matter and nerve pathways known as the corpus callosum. The corpus callosum occupies a central position within the cerebrum.

- The **Brainstem** is located beneath the cerebrum and in front of your cerebellum and it connects the brain to the spinal cord. It controls automatic functions such as breathing, digestion, heart rate and blood pressure and it includes three primary structures: the **midbrain**, the **pons**, and the **medulla**.

  – The **midbrain** is a small region of the brainstem and it serves as a vital link between various parts of the central nervous system, playing an essential role in sensory and motor functions.

    Anatomically, the midbrain consists of two main structures: the tectum and the tegmentum. The tectum is located dorsally and is further divided into the superior colliculi and inferior colliculi. These structures are involved in visual and auditory processing, respectively. The superior colliculi primarily coordinate visual reflexes and eye movements, while the inferior colliculi are responsible for auditory processing, including sound localization and integration of auditory information.
    The tegmentum, located ventrally to the tectum, contains several important nuclei and fiber tracts. It includes the red nucleus, substantia nigra, and the periaqueductal gray. The red nucleus is involved in motor coordination, particularly in the control of limb movements. The substantia nigra plays a crucial role in the production of dopamine and is primarily associated with motor functions and reward mechanisms. Dysfunction of the substantia nigra is linked to Parkinson's disease, a neurodegenerative disorder characterized by motor impairments. The periaqueductal gray is involved in pain modulation and the autonomic control of vital functions.
    The midbrain also contains various ascending and descending fiber tracts that facilitate communication between different parts of the brain. Notably, the cerebral peduncles are large fiber tracts located ventrally in the midbrain, connecting the cerebral cortex with the spinal cord and facilitating motor control and coordination.
    In addition to its sensory and motor functions, the midbrain is involved in regulating sleep-wake cycles, arousal, and attention. It also participates in the control of eye movements and pupil dilation. Moreover, the midbrain serves as a relay center for transmitting information between higher brain regions and the spinal cord.

  – The **pons** is a structure located in the brainstem, specifically between the midbrain and the medulla oblongata. It serves as a vital relay center, connecting various regions of the brain and facilitating communication between different parts of the central nervous system [30].

    Functionally, the pons plays a crucial role in several important processes:

    1. Relay of Information: The pons serves as a bridge between the cerebrum, cerebellum, and spinal cord. It contains numerous nerve fibers that transmit sensory and motor information between these regions [31].
    2. Respiratory Control: Within the pons, there are specialized nuclei involved in regulating respiration. These nuclei coordinate the timing and pattern of breathing, ensuring the smooth functioning of the respiratory system [32].
    3. Sleep Regulation: The pons contributes to the regulation of sleep and arousal. It contains nuclei involved in the generation of rapid eye

movement (REM) sleep, a stage of sleep associated with dreaming and heightened brain activity [33].

4. Motor Control: Certain motor pathways pass through the pons, allowing for the coordination of voluntary movements. The pons is involved in the control of facial expressions, eye movements, and posture [34].
5. Sensory and Motor Integration: By connecting different regions of the brain, the pons facilitates the integration of sensory information and motor output. This integration is essential for coordinating complex movements and maintaining overall body balance [35].
   In summary, the pons serves as a vital hub for relaying information, regulating respiration and sleep, coordinating motor functions, and integrating sensory and motor signals. Its location in the brainstem underscores its importance in fundamental physiological processes.

– The **medulla oblongata**, commonly referred to as the **medulla**, is a vital part of the brainstem located between the pons and the spinal cord. It plays a crucial role in regulating several essential bodily functions necessary for survival [36].
  Here is some key information about the medulla:

  1. Autonomic Functions: The medulla controls various autonomic functions that are critical for maintaining homeostasis. It regulates vital processes such as heart rate, blood pressure, and respiration. Specific nuclei within the medulla, such as the cardiovascular and respiratory centers, help monitor and adjust these functions to meet the body's needs [37].
  2. Reflexes: The medulla is involved in coordinating many important reflex actions. It integrates sensory information from the cranial nerves and the spinal cord to initiate reflex responses. Examples of medullary reflexes include the gag reflex, coughing, sneezing, and swallowing [31].
  3. Cranial Nerve Nuclei: The medulla contains several nuclei associated with cranial nerves. These nuclei serve as the origin or termination points for the cranial nerves, which control various sensory and motor functions of the head and neck. Examples include the nuclei for the glossopharyngeal nerve (CN IX), vagus nerve (CN X), and hypoglossal nerve (CN XII) [37].
  4. Pyramidal Decussation: Within the medulla, the corticospinal tracts undergo a crucial crossover called the pyramidal decussation. This means that motor signals originating in one cerebral hemisphere cross over to the opposite side of the body. This decussation enables the medulla to play a significant role in voluntary motor control and coordination [38].
  5. Reticular Formation: The medulla contains a part of the reticular formation, a network of interconnected neurons that regulate consciousness, arousal, and sleep-wake transitions. The medullary reticular formation helps maintain alertness and regulates the sleep-wake cycle [34].
     The medulla oblongata is a critical structure in the brainstem responsible for controlling autonomic functions, coordinating reflexes, housing cranial nerve nuclei, facilitating motor control, and contributing

to the regulation of consciousness and sleep-wake cycles. Its integration of various functions makes it an indispensable component for overall bodily homeostasis.

- The **Cerebellum**, often referred to as the "little brain," is a compact structure positioned at the posterior part of the head, situated beneath the temporal and occipital lobes and above the brainstem. Similar to the cerebral cortex, it is divided into two hemispheres. The outer region consists of neurons, while the inner area communicates with the cerebral cortex.

  The primary function of the cerebellum is to coordinate voluntary muscle movements and contribute to the maintenance of posture, balance, and equilibrium. However, recent studies are delving into the broader roles of the cerebellum, exploring its potential involvement in cognition, emotions, social behavior, and its potential link to conditions such as addiction, autism, and schizophrenia. These investigations seek to unravel the intricate contributions and significance of the cerebellum beyond its traditionally recognized motor functions.

2.3 Electroencephalography (EEG)

EEG (electroencephalography) is a non-invasive neuroimaging technique that measures the electrical activity of the brain. It was developed by German physicist and psychiatrist Hans Berger in 1924 and it involves placing electrodes on the scalp to detect and record the electrical signals generated by the activity of neurons. EEG has a high temporal but low spatial resolution which means that EEG recordings are capable of capturing and detecting rapid changes in brain activity over time with great precision, providing detailed information about the timing and sequence of neural processes. However, low spatial resolution means that the EEG recordings that have limited capability to precisely localize and identify the specific brain regions or sources contributing to the recorded electrical activity. Spatial resolution in EEG refers to the ability to accurately pinpoint the origin and location of brain activity [39].

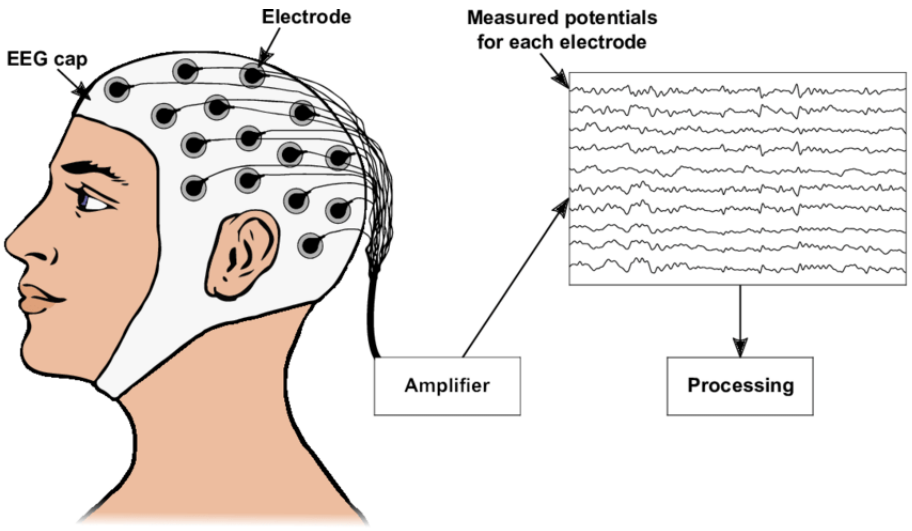

FIGURE 2.5: Recording of an Electroencephalogram

During the initial stages of development, EEG signals were recorded using galvanometers. However, advancements in modern electronic circuitry have led to a shift in signal recording methods. Presently, a combination of electrodes, differential amplifiers for each channel, and filters are employed. As the number of channels increases, so does the computational complexity. The quality of EEG signals is influenced by various factors, including the type of electrode used. Previous research has highlighted different electrode types utilized in EEG recording, including disposable electrodes (gel-less and pre-gelled), reusable disc electrodes, headbands and electrode caps, saline-based electrodes, and needle electrodes [40]. Typically, electrodes employed in clinical and research settings are made of Ag-AgCl material and have a diameter smaller than 3 mm. These electrodes are connected to the amplifier through lengthy wires, enabling the amplification of small electrical signals obtained from the scalp. In invasive cases, needle electrodes are inserted into the skull through a minor surgical procedure [41]. To optimize the recording of EEG signals, it is important to maintain the electrode impedance within the range of 1 to 5 KΩ. Figure 2.6 illustrates examples of sample EEG signals.

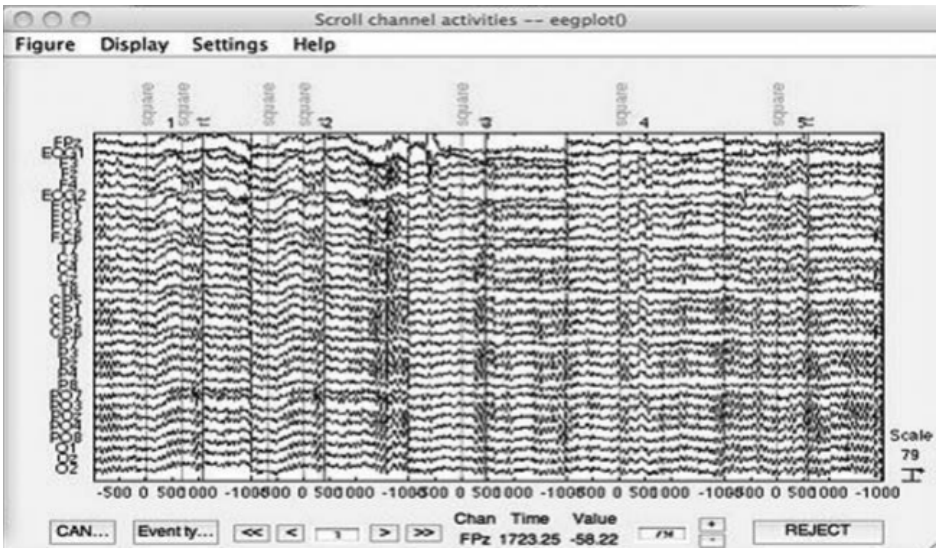

FIGURE 2.6: Sample EEG recording signals

2.4 The 10–20-electrode placement system

In 1958, a standardized method for electrode placement in EEG was introduced, based on anatomical landmarks on the head [42, 43, 44]. This system, known as the 10-20 electrode placement system, was initially approved by the International Federation of Societies for Electroencephalography and Clinical Neurophysiology for 21 electrodes. In this arrangement, odd-numbered electrodes are positioned on the left side of the head, while even-numbered electrodes are placed on the right side. To accommodate a larger number of electrodes (e.g., 128, 256, 512, etc.), additional electrodes can be inserted with equal spacing between existing electrodes.

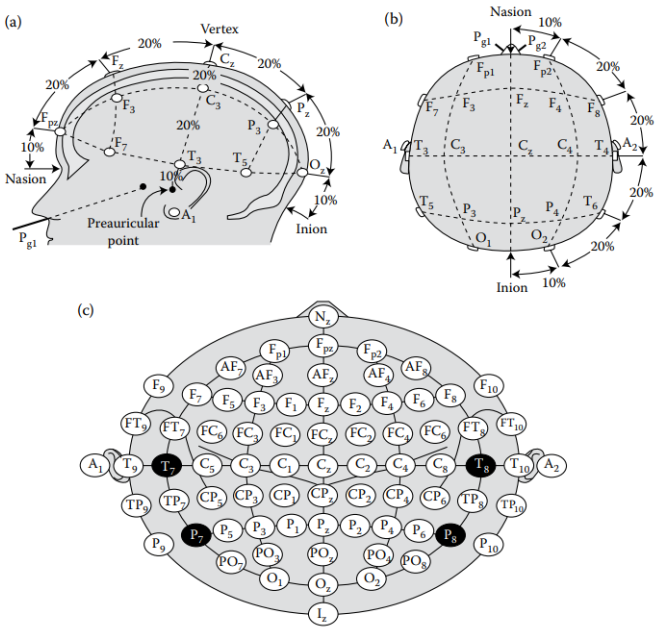

FIGURE 2.7: Diagrammatic view of the 10–20-electrode system [45]

Figure 2.7 illustrates a diagrammatic representation of the 10–20-electrode system, displaying the distances between various regions of the head and the placement of 75 electrodes, including reference electrodes. Traditionally, the electrodes connected to the ear lobes (A1 and A2) have been commonly used as reference electrodes. However, in modern instrumentation, the choice of reference does not have a significant impact on the measurement process [46]. Alternative reference options, such as FPz, hand, or leg electrodes, can be utilized in these systems [47]. The standard nomenclature for electrode placement is as follows: A for earlobe, O for occipital, P for parietal, F for frontal, and Fp for frontal polar regions.

Chapter 3

Source Analysis

3.1 EEG Source Analysis

EEG (electroencephalography) is a non-invasive technique that measures the electrical activity of the brain through electrodes placed on the scalp. One of the main challenges in interpreting EEG signals is to identify the underlying neural sources responsible for generating the measured scalp potentials. This is known as EEG source analysis or EEG inverse problem. Source analysis techniques aim to reconstruct the neural activity in the brain that gives rise to the observed EEG signals. One commonly used approach is dipole fitting, which involves modeling the brain as a collection of current dipoles and estimating their locations and strengths to match the observed scalp potentials [1]. Another approach is distributed source modeling, which estimates the distribution of current sources across the brain volume or cortical surface based on the measured EEG data [48]. EEG source analysis has important applications in neuroscience and clinical neurology. It allows researchers to investigate the spatiotemporal dynamics of neural activity underlying cognitive and perceptual processes [49]. It also enables the localization of abnormal brain activity in patients with epilepsy, tumors, or other neurological disorders, which can guide surgical planning and treatment [2]. In addition, EEG source analysis has been used to identify biomarkers of cognitive impairment and Alzheimer's disease [50]. Despite its potential, EEG source analysis has limitations and challenges. One major challenge is the ill-posed nature of the inverse problem, which means that multiple possible brain source configurations can give rise to the same scalp potentials [51]. This ambiguity can lead to inaccurate or unreliable source estimates, especially in noisy or complex EEG data. Another challenge is the integration of EEG with other neuroimaging techniques such as fMRI and MEG to study brain networks and interactions [52, 53].

3.2 Forward Problem

In the context of brain source analysis, the forward problem refers to the challenge of determining how electrical or magnetic signals measured on the scalp, such as in electroencephalography (EEG) or magnetoencephalography (MEG), are generated by neural activity within the brain.

When neural activity occurs in the brain, it generates electrical currents or magnetic fields that propagate through the brain and surrounding tissues. These signals can be measured non-invasively using external sensors placed on the scalp. The forward problem involves solving the mathematical equations that describe the relationship between the neural sources and the measured signals, in order to understand how the activity of specific brain regions gives rise to the observed scalp measurements.

Solving the forward problem requires constructing a model of the head and brain that accounts for factors such as the conductivity properties of different tissues, the geometry of the head, and the positions of the sensors. The model is used to simulate the flow of electrical currents or magnetic fields generated by neural sources and predict how these fields will be detected by the scalp sensors. The goal is to accurately simulate the observed measurements based on the known or estimated neural sources.

Accurately solving the forward problem is essential for various neuroimaging applications, such as source localization and functional connectivity analysis. By estimating the neural sources responsible for the measured signals, researchers can infer the spatial distribution of neural activity within the brain. This information is valuable for understanding brain function, studying cognitive processes, and investigating neurological disorders.

It's worth noting that the forward problem is closely related to the inverse problem in brain source analysis. While the forward problem aims to predict the scalp measurements based on known or estimated neural sources, the inverse problem seeks to estimate the neural sources given the measured scalp data. The forward and inverse problems are intertwined and often require iterative approaches to achieve more accurate and reliable results.

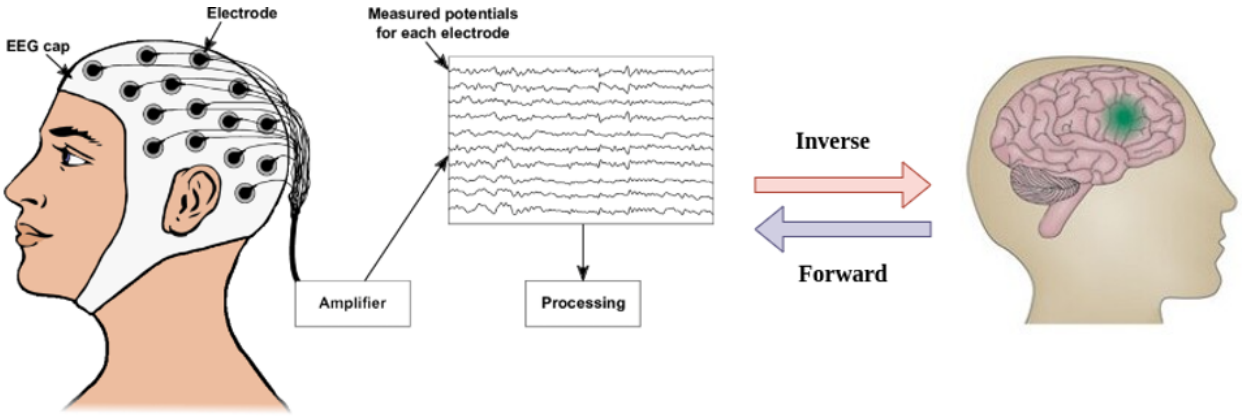

3.3 Mathematical background for the forward problem

For p dipoles and q electrodes and for each time point:

$$\mathbf{X} = \mathbf{LS} \tag{3.1}$$

where, $X \in \mathbb{R}^{q \times t}$ is the estimated EEG channel measurements over time t, $L \in \mathbb{R}^{q \times p}$ is the leadfield matrix that describes the flow of electrical current of each dipole through every electrode and $S \in \mathbb{R}^{q \times t}$ represents the electrical current of each dipole over time.

For a specific time point t_k, the above equation becomes:

$$X_{est_k} = \underbrace{\begin{bmatrix} X_{est}(electrode_1)_k \\ \vdots \\ X_{est}(electrode_q)_k \end{bmatrix}}_{q \times 1} = \underbrace{\begin{bmatrix} g(r_1, r_{dip_1}) & \dots & g(r_1, r_{dip_p}) \\ \vdots & \ddots & \vdots \\ g(r_q, r_{dip_1}) & \dots & g(r_q, r_{dip_p}) \end{bmatrix}}_{q \times p} \underbrace{\begin{bmatrix} d_1 e_1 \\ \vdots \\ d_p e_p \end{bmatrix}}_{p \times 1} \tag{3.2}$$

where $r_1, ..., r_q$ are the positions of each electrode and $r_{dip_1}, ..., r_{dip_p}$ are the positions of each dipole in the source space.

A noise matrix $\mathbf{n}$ is added to equation (5.2):

$$\mathbf{X} = \mathbf{LS} + \mathbf{n} \tag{3.3}$$

The noise is modeled as a Gaussian random variable with zero mean and standard deviation σ:

$$\mathbf{n} \sim \mathcal{N}(0, \sigma^2 \mathbf{I}_q) \tag{3.4}$$

where $\mathbf{I}_q$ is the identity matrix

3.3.1 Maxwell's equations

In order to solve the EEG forward problem, it is important to understand Maxwell's equations. This section explains the mathematical formulation for all Maxwell equations, which are termed as Maxwell's equations for electromagnetics, as they define the relationship between electrical and magnetic quantities in terms of time-varying derivations.

James Maxwell formulated the interconnection among different electrical and magnetic quantities in 1861, establishing a pivotal contribution to electromagnetism. His work resulted in a set of equations now known as Maxwell's equations, which describe the relationship between electromagnetic fields, charge density, and current density. These equations exist in two forms: the point or differential form and the integral form, offering alternative representations of the same fundamental principles.

The equations developed by Maxwell find applications in examining the dynamic characteristics of electric and magnetic fields in different materials. These equations are influenced by properties like the permittivity, the permeability, the conductivity, and the impedance of the medium. [book citation]

Differential form

$$\nabla \times \mathbf{H} = \frac{\partial D}{\partial t} + \mathbf{J} \quad \text{(Ampere's law)} \tag{3.5}$$

$$\nabla \times \mathbf{E} = -\frac{\partial B}{\partial t} \quad \text{(Faraday's law)} \tag{3.6}$$

$$\nabla \cdot \mathbf{D} = \rho_v \quad \text{(Gauss's law)} \tag{3.7}$$

$$\nabla \cdot \mathbf{B} = 0 \quad \text{(Gauss's law for magnetism)} \tag{3.8}$$

Integral form

$$\oint_L \mathbf{H} \cdot d\mathbf{L} = \int_S \left(\frac{\partial D}{\partial t} + \mathbf{J} \right) dS \tag{3.9}$$

$$\oint_L \mathbf{E} \cdot d\mathbf{L} = -\int_S \frac{\partial \mathbf{B}}{\partial t} + \mathbf{J} \Big) dS \tag{3.10}$$

$$\oint_S \mathbf{D} \cdot dS = \oint_v \rho_v \, dv \tag{3.11}$$

$$\oint_S \mathbf{B} \cdot d\mathbf{S} = 0 \tag{3.12}$$

where $\mathbf{H}$ = magnetic field strength (A/m), $\mathbf{E}$ = electric field strength (V/m), $\mathbf{D}$ = electric flux density (C/m^2), $\frac{\partial D}{\partial t}$ = displacement electric current density (A/m^2), J = conduction current density (A/m^2) , B = magnetic flux density $(wb/m^2$or Tesla), $\frac{\partial B}{\partial t}$ = time-derivative of magnetic flux density $(wb/m^2 s$, ρ_v = Volume charge density (C/m^3), dL = differential length, dS = differential area, and $d\rho_v$ = differential volume.

The above equations can be understood within the framework of a dynamic electric or magnetic field. For instance, Equation (3.13), which corresponds to Ampere's law, describes how alterations in magnetomotive force along a closed path lead to the accumulation of electric displacement and conduction currents through any surface that encloses the path.The next equation, often referred to as Faraday's law, articulates that the electromotive force encircling a closed path is equivalent to the negative rate of change of magnetic flux traversing any surface encompassed by the path. Maxwell's third equation, also known as Gauss' law, establishes the connection between electric displacement flux and the total charge contained within that surface. Lastly, we have Gauss' law for magnetism, which asserts that the total magnetic flux crossing any closed surface amounts to zero.[54],[55],[56] The equations mentioned above have various formulations tailored to different types of media, such as homogeneous, nonhomogeneous, isotropic, anisotropic, and source-free regions. This is because the properties of the medium, such as permittivity ε, permeability μ, and conductivity σ, vary significantly across different mediums. For instance, in free space where the relative permittivity (ε_r) is 1, relative permeability (μ_r) is 1, there is no conduction current density (J), and conductivity is zero, the set of Maxwell's equations can be expressed as follows [57],[58],[59],[60]:

$$\nabla \times \mathbf{H} = \frac{\partial D}{\partial t} \leftrightarrow \oint_L \mathbf{H} \cdot dL = \int_S \frac{\partial D}{\partial t} dS \tag{3.13}$$

$$\nabla \times \mathbf{E} = -\frac{\partial B}{\partial t} \leftrightarrow \oint_L \mathbf{E} \cdot dL = -\int_S \frac{\partial B}{\partial t} \cdot dS \tag{3.14}$$

$$\nabla \cdot \mathbf{D} = 0 \leftrightarrow \oint_S \mathbf{D} \cdot dS = \int_v \rho_v \, dv \tag{3.15}$$

$$\nabla \cdot \mathbf{B} = 0 \leftrightarrow \oint_S \mathbf{B} \cdot dS = 0 \tag{3.16}$$

3.3.2 Quasi-static approximation for head modeling

Neuroscientists primarily focus on a frequency range below 1 kHz when studying the brain and therefore the majority of studies involve frequencies ranging from 0.1 to 100 Hz. As a result, the physics associated with magnetoencephalography/EEG can be adequately described using quasi-static approximations of Maxwell's equations. This approximation remains valid since brain signals predominantly occur at lower frequencies. At these lower frequencies, the time-derivative aspect of Maxwell's equations is ignored. This approximation for Maxwell's equations is known as the quasi-static approximation. This approximation has been established and verified through literature reviews, such as the work conducted by Hämäläinen and Sarvas [12]. Consequently, assuming that the head tissues exhibit the permeability of free space, the form of Maxwell's equations is modified as follows:

$$\nabla \times \mathbf{B} = \mu_0 \mathbf{J} + \mu_0 \varepsilon_r \varepsilon_0 + \frac{\partial E}{\partial t} \tag{3.17}$$

where ε is the medium permittivity and μ is the permeability. These values change significantly for various mediums.

$$\nabla \times \mathbf{E} = -\frac{\partial B}{\partial t} \tag{3.18}$$

$$\nabla \cdot \mathbf{E} = \frac{\rho}{\varepsilon_r \varepsilon_0} \tag{3.19}$$

$$\nabla \cdot \mathbf{B} = 0 \tag{3.20}$$

Using Ohm's law, $\mathbf{J} = \sigma \mathbf{E}$, equation (3.17) becomes:

$$\nabla \times \mathbf{B} = \mu_0 \left(\sigma \mathbf{E} + \varepsilon_r \varepsilon_0 + \frac{\partial E}{\partial t} \right) \tag{3.21}$$

In Ohms law, σ is the position dependent conductivity.The conductivity σ of a material is influenced by factors such as its composition, the arrangement of its

components, and its temperature [97]. When dealing with isotropic conductivities, the conductivity can be described as a scalar quantity that depends on position (x, y, z). However, in the case of anisotropic conductivities, the conductivity is represented by a position-dependent second-order tensor σ. This tensor, denoted as $\sigma(x, y, z) \in \mathbb{R}^{3\times3}$, can be expressed as a 3x3 matrix in a basis (e_x, e_y, e_z).

$$\sigma = \begin{bmatrix} \sigma_{xx} & \sigma_{xy} & \sigma_{xz} \\ \sigma_{yx} & \sigma_{yy} & \sigma_{yz} \\ \sigma_{zx} & \sigma_{zy} & \sigma_{zz} \end{bmatrix} \tag{3.22}$$

After combining $\mathbf{E}(t) = \mathbf{E}_0 \cdot e^{-j\omega t}$ with equation (3.21) we get:

$$\nabla \times \mathbf{B} = \mu_0(\sigma\mathbf{E} - j\varepsilon_0\varepsilon_r\omega\mathbf{E}) \tag{3.23}$$

Thus, for a quasi-static approximation, it holds that

$$\left|\frac{\varepsilon_0\varepsilon_r}{\sigma}\right| \ll 1 \tag{3.24}$$

because, according to [61], the tissue conductivity for the head region at a frequency of $100Hz$ is $0.3\Omega^{-1}m^{-1}$ with relative permittivity $\varepsilon_r = 105$.

We can apply a similar analogy to the second equation, $\nabla \times \mathbf{E} = -\frac{\partial B}{\partial t}$ in which the temporal derivative of magnetic field strength (**B**) can be neglected because of low frequencies thus:

$$\nabla \times \mathbf{E} = 0 \tag{3.25}$$

The use of quasi-static assumptions simplifies the mathematical analysis as it separates the magnetic and the electric field calculations. Additionally, the time delay of the neural signals transmitted by the active sources inside the brain to the electrodes on the scalp can be ignored and therefore the brain activity is captured without any delay.[62] Based on the analysis of Maxwell's equation under the assumption of quasi-static conditions, it was deduced that the curl of the electric field intensity is equal to zero. As a result, we can establish a connection between the gradient of the scalar potential V and the field strength in the following manner:

$$\mathbf{E} = -\nabla\mathbf{V} \tag{3.26}$$

The total current density **J** in a volume with current generators can be divided into two distinct components:

- The primary current flow, $\mathbf{J^P}$ which is the current density due to the neuronal activity in the brain. This current density is spatially bounded in a volume
- The volume currents, $\mathbf{J^v}$. The electric field in the volume that is being observed is what causes the volume current density to flow.

By making use of the point form of Ohm's law,

$$\mathbf{J^v} = \sigma\mathbf{E} \tag{3.27}$$

the total current density is given as follows:

$$\mathbf{J} = \mathbf{J^P} + \mathbf{J^v} = \mathbf{J^P} + \sigma\mathbf{E} = \mathbf{J^P} - \sigma\nabla\mathbf{V} \tag{3.28}$$

Equation (3.23) can be written as follows:

$$\begin{aligned} &\nabla \times \mathbf{B} = \mu_0 \sigma \mathbf{E} = \mu \mathbf{J} \\ &\nabla \cdot (\nabla \times \mathbf{B}) = \nabla \cdot (\mu \mathbf{J}) \Rightarrow \\ &\nabla \cdot (\mu \mathbf{J}) = 0 \Rightarrow \\ &\boxed{\nabla \cdot (\mathbf{J}) = 0} \end{aligned} \tag{3.29}$$

From (3.28) we get that

$$\begin{aligned} \mathbf{J} &= \mathbf{J^P} - \sigma \nabla \mathbf{V} \\ \nabla \cdot (\mathbf{J}) &= \nabla \cdot (\mathbf{J^P}) - \nabla \cdot (\sigma \nabla \mathbf{V}) \end{aligned} \tag{3.30}$$

But from (3.29), $\nabla \cdot (mathbf J) = 0$ and therefore

$$\begin{aligned} 0 &= \nabla \cdot (\mathbf{J^P}) - \nabla \cdot (\sigma \nabla \mathbf{V}) \\ \nabla \cdot (\mathbf{J^P}) &= \nabla \cdot (\sigma \nabla \mathbf{V}) \end{aligned} \tag{3.31}$$

The equation $\nabla \cdot (\mathbf{J^P}) = \nabla \cdot (\sigma \nabla \mathbf{V}$ is known as Poisson's equation for the electric potential $\mathbf{V}$ inside an isotropic medium with arbitrary conductivity and insulated boundary. $\mathbf{J}$ symbolizes the current density, which is a three-dimensional vector field $\mathbf{J}(x, y, z)$ measured in A/m^2

By taking the divergence of this vector field, we generate the current source density which is symbolized with $\mathbf{I}_m$ and has units of A/m^3. Therefore,

$$\nabla \cdot (\mathbf{J^P}) = \nabla \cdot (\sigma \nabla \mathbf{V}) = \mathbf{I}_m \tag{3.32}$$

which constitutes the forward problem equation for EEG source localization. Given a specific head model and current source, (3.32) can be used to evaluate both the electric potential that satisfies the equation at every point within the head volume conductor model and address the forward problem effectively. [63]

When there is no free charge, Poisson's equation (3.32) takes the following form, which is know as the Laplace equation for EEG source analysis.

$$\nabla \cdot (\sigma \nabla \mathbf{V}) = 0 \tag{3.33}$$

3.3.3 Boundary conditions

The are two boundary conditions that need to be satisfied in order to solve the forward problem for EGG source localization, as described by the above Laplace equation 3.33.These conditions are referred to as Neumann and Dirichlet boundary conditions, and they are applied at the interfaces between two different regions. The distinction between these regions is determined by their respective conductivities (σ_1 and σ_2), and the unit normal vector n' denotes the direction perpendicular to the interface between the two regions.

The Neumann boundary condition implies that charges do not accumulate at the interfaces but rather continue to move after leaving one interface. In simpler terms, since the head acts as a purely resistive medium, the current flows continuously from one interface to another. Therefore, all the current that leaves a region with conductivity σ_1 through the interface enters the neighboring region with conductivity σ_2.

This can be expressed mathematically as follows:

$$\begin{aligned} \mathbf{J}_1 \cdot n &= \mathbf{J}_2 \cdot n \\ (\sigma_1 \nabla \mathbf{V_1}) \cdot n' &= (\sigma_2 \nabla \mathbf{V_2}) \cdot n' \end{aligned} \tag{3.34}$$

where n' is the normal vector on the interface.

The homogeneous Neumann boundary condition is a specific instance of the Neumann boundary condition and is applicable when dealing with a homogeneous medium.[64] In this case, it is specifically applied at the outer surface of the human head. The condition states that no current is allowed to flow from the head into the surrounding air due to the low conductivity of air. Mathematically:

$$\begin{aligned} \mathbf{J}_1 \cdot n' &= 0 \\ (\sigma_1 \nabla \mathbf{V_1}) \cdot n' &= 0 \end{aligned} \tag{3.35}$$

The other boundary condition used in solving the forward problem which is known as the Dirichlet boundary condition, is applied specifically to internal interfaces. It provides information about the potential (electric potential) at the boundary and it states that the electric potential remains continuous across these interfaces, meaning that there are no abrupt changes in potential. This can be expressed as follows:

$$\mathbf{V_1} = \mathbf{V_2} \tag{3.36}$$

The above equation corresponds to the Dirichlet boundary condition. An electrode with zero potential is used as a reference and it assigned in such a way that

$$\mathbf{V_{ref}} = 0 \tag{3.37}$$

Therefore, when addressing the forward problem and calculating the potential caused by dipole sources in various head models, it is essential to incorporate the mentioned boundary conditions. By doing so, a more accurate solution can be achieved, minimizing errors and enhancing the level of resolution.

3.3.4 Conductivity

When modeling the head, its characteristics rely on both its geometry and conductivity. Isotropic conductivity means that the conductivity is equal in all directions as opposed to anisotropic conductivity where the conductivity can differ depending on the direction that the current flows. An isotropic conductivity is used in most cases despite the fact that the conductivity of the skull and white matter is an anisotropic one.[65]

Anisotropic conductivities

The human skull refers to the entire bony structure that forms the head and protects the brain, as well as the sensory organs, facial structures, and other important structures within the head. It is comprised of several bones that are interconnected to create a rigid framework that surrounds and protects the brain from external injuries and provide structural support to maintain the brain's integrity. Therefore, the skull constitutes a hard structure which acts a poor conductor and has a layered composition as shown in figure 3.1 below:, which comprises of three layers: two

hard layers that have a spongy layer between them. Water and ionized particles can move freely through the middle spongiform layer but they are unable to pass through the hard layers. This is shown in figure 3.2. The conductivity that is tangent to the surface is 10 times greater than the conductivity that is perpendicular.[66]

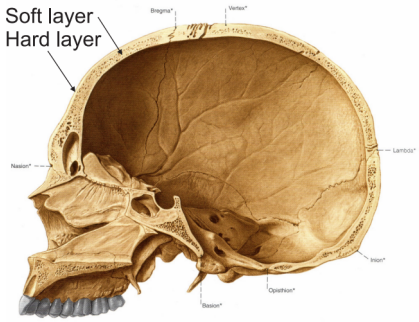

FIGURE 3.1: The image displays a sagittal perspective of the skull, revealing the distinct layers of soft and hard tissues. Notable anatomical landmarks on the skull are highlighted, including the inion and nasion. These specific points are commonly utilized in clinical settings for electrode placement on the scalp. This depiction has been adapted from Putz and Pabst.

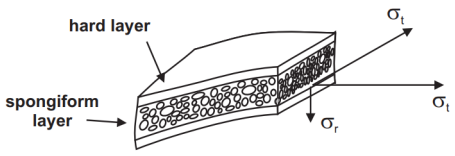

FIGURE 3.2: anisotropic properties of the conductivity of skull

3.4 Head modeling

Head modeling in EEG source analysis is an essential step in understanding the electrical activity of the brain. It involves creating a computational model of the head and its various tissues to accurately simulate and localize the sources of electrical signals recorded from the scalp using electroencephalography (EEG).

The main goal of head modeling in EEG source analysis is to estimate the location and strength of brain activity generating the recorded EEG signals. To achieve this, a realistic representation of the head geometry and conductivity distribution is necessary. There are two primary components involved in head modeling for EEG source analysis:

1. Head Geometry: This component focuses on capturing the shape and structure of the head, including the scalp, skull, and brain. Various techniques such as magnetic resonance imaging (MRI) or computed tomography (CT) are used to acquire high-resolution head images. These images are then processed to extract the head geometry information, typically represented as a three-dimensional (3D) mesh.

2. Conductivity Model: Different tissues in the head exhibit varying electrical conductivities. To account for this, a conductivity model is created to assign

appropriate conductivity values to different regions, such as the scalp, skull, cerebrospinal fluid, and brain. These conductivity values are important because they affect the propagation and distribution of electrical signals within the head.

Once the head model is constructed, it is incorporated into the EEG source analysis pipeline to estimate the neural sources of the recorded EEG signals. This typically involves solving the inverse problem, which aims to find the brain activity that best explains the recorded data. Different inverse methods, such as dipole fitting, distributed source models, or beamforming, can be used to estimate the location and strength of the underlying brain sources.

Accurate head modeling is crucial for obtaining reliable and interpretable results in EEG source analysis. It allows researchers and clinicians to localize and study brain activity related to various cognitive processes, neurological disorders, or clinical conditions. Advances in imaging technologies and computational techniques continue to improve the accuracy and sophistication of head modeling in EEG source analysis, enhancing our understanding of the brain's electrical activity.

3.4.1 Quasistatic assumptions

MEG and EEG forward modeling also consists in identifying the influence of the head geometry and of the electromagnetic properties of its tissues on data formation. This last step is popularly coined "head modeling". For a given model of elementary neural currents and sensor array, the physics of MEG and EEG are ruled by the theory of electrodynamics (Feynman, 1964), which reduces in MEG to Maxwell's equations, and to Ohm's law in EEG, under quasistatic assumptions. These latter consider that the propagation delay of the electromagnetic waves from brain sources to the MEG/EEG sensors is negligible. The reason is the relative proximity of MEG/EEG sensors to the brain with respect to the expected frequency range of neural sources (up to 1 kHz) (Hämäläinen et al., 1993). This is a very important, simplifying assumption, which has immediate consequences on the computational aspects of MEG/EEG head modeling. Indeed, the equations of electro- and magneto-statics determine that there exist analytical, closed-form solutions to MEG/EEG head modeling when the head geometry is considered spherical. Hence, the simplest, and consequently by far most popular model of head geometry in MEG/EEG consists of concentric spherical layers: with one sphere per major category of head tissue (scalp, skull, cerebrospinal fluid and brain).[67]

3.4.2 Simplified, spherical head geometry

The spherical head geometry has further attractive properties for MEG in particular. Quite remarkably indeed, spherical MEG head models are insensitive to the number of shells and their respective conductivity: a current source within a single homogeneous sphere generates the same MEG fields as when located inside a multilayered set of concentric spheres with different conductivities. The reason for this is that conductivity only influences the distribution of secondary volume currents that circulate within the head volume and which are impressed by the original primary neural currents. The analytic formulation of Maxwell's equations in the spherical geometry demonstrates that these secondary currents do not generate any magnetic field outside the volume conductor (Sarvas, 1987). Consequently, the conductivity and radius of each spherical layer have no influence on the measured MEG fields, which is not the case in EEG. This is considered a major advantage for MEG.

Geometrical registration to individual MRI anatomical data improves the adjustment of the best-fitting sphere geometry to the participant's head. A spherical head model can be optimally adjusted to the head geometry, or restricted to regions of interest e.g., posterior regions for visual studies. Another remarkable consequence of the spherical symmetry is that radially oriented brain currents produce no magnetic field outside a spherically symmetric volume conductor. For this reason, MEG signals from currents generated at the gyral crests or sulcal depths are attenuated, with respect to those generated by currents flowing perpendicularly to the sulcal walls. The difference in sensitivity to source orientation is another important contrast between MEG and EEG (Hillebrand and Barnes, 2002). Finally, the amplitude of magnetic fields decreases faster than electrical potentials' with the distance from the generators to the sensors. Hence it has been argued that MEG is less sensitive to mesial and subcortical brain structures than EEG. An increasing body of experimental evidence and modeling efforts has shown however that MEG can detect neural activity from deeper brain regions (Attal and Schwartz, 2013).[67]

3.4.3 Realistic head geometry

Although spherical head models are convenient, they are poor approximations of the human head shape, which impacts the accuracy of MEG/EEG source estimation (Stenroos et al., 2012). The use of more realistic head geometries, which requires solving Maxwell's equations with numerical methods, has also been proposed. Boundary Element (BEM) and Finite Element (FEM) methods are generic numerical approaches to the resolution of continuous equations over discrete space. In MEG/EEG, geometric tessellations of the different envelopes forming the head tissues need to be extracted from the individual MRI volume data to yield a realistic approximation of their geometry. In BEM, the conductivity of tissues is supposed to be homogeneous and isotropic within each envelope. Therefore, each tissue envelope is delimited using surface boundaries defined over a triangulation of each of the segmented envelopes obtained from MRI. FEM assumes that tissue conductivity may be anisotropic (such as the skull bone and the white matter); therefore the primary geometric building block needs to be an elementary volume, such as a tetrahedron (Marin et al., 1998). In practice, the FEM's tessellation step remains tedious and complicated. However, efficient implementations of BEM have been derived recently (e.g., Kybic et al, 2005) and are now readily available in several commercial and academic software applications (Baillet et al., 2011). An important caveat, especially for EEG: Realistic head modeling also depends on the correct estimation of tissue conductivity values, which are difficult to access in vivo. Methods of impedance tomography have been proposed with MRI (Tuch et al., 2001) and EEG (Goncalves et al., 2003) but have had limited practical impact so far. Hence, conductivity values from ex-vivo models are conventionally considered in MEG and EEG head models (Geddes and Baker, 1967).[67]

3.5 Boundary Element Method

The Boundary Element Method (BEM) is a numerical technique used for solving partial differential equations (PDEs) and boundary value problems. It is particularly well-suited for problems involving Laplace's equation and its variants, such as Poisson's equation and Helmholtz's equation.

BEM focuses on discretizing the boundary of the problem domain rather than the

entire domain. It represents the solution to the PDE as an integral equation over the boundary, which is then solved to obtain the unknown distribution of the solution. This approach reduces the dimensionality of the problem and can lead to computational efficiency compared to methods that require discretization of the entire domain.

BEM has several advantages. It can handle problems with infinite or unbounded domains since the boundary is the primary focus. It is particularly useful for problems where the solution is smooth inside the domain but has complex behavior near the boundaries. BEM also provides accurate solutions for problems with singularities, such as problems with point sources or corners.

However, BEM also has some limitations. It is generally more suitable for problems with homogeneous materials and linear PDEs. It can struggle with problems involving nonlinearities or problems with changing boundary conditions. Additionally, BEM requires the computation of boundary integrals, which can be challenging and time-consuming in certain cases.

3.6 Boundary Element Method and EEG

The Boundary Element Method (BEM) is a numerical technique used for solving partial differential equations (PDEs) in domains with complex boundaries [68]. It is particularly useful for problems involving electromagnetic fields, such as in electroencephalography (EEG) source analysis.

EEG source analysis is a method used to estimate the underlying neural sources of EEG signals measured on the scalp [69]. It aims to localize the brain activity responsible for generating the measured EEG data. BEM can be employed in EEG source analysis to solve the forward problem, which involves calculating the electric potential distribution on the scalp resulting from a known distribution of current sources within the brain [70].

In EEG source analysis, BEM is often used to model the head as a multi-layered spherical or realistic head model [65]. The boundary surfaces of the head model, such as the scalp, skull, and brain, are discretized into small elements. BEM then approximates the solution of the electric potential distribution by formulating integral equations that relate the potential at each element to the known sources and the potential on the boundary elements [71].

The BEM formulation in EEG source analysis typically involves solving the Laplace or Poisson equation, depending on the assumptions made about the electrical conductivity distribution in the head model. By solving these equations, BEM can provide an estimation of the electric potential at the scalp surface resulting from neural activity within the brain [72].

Once the forward problem is solved using BEM, it is possible to further analyze the EEG data to localize the sources of neural activity. This can be achieved through inverse methods, such as dipole fitting or distributed source modeling, which aim to estimate the locations and strengths of the underlying sources based on the measured scalp potentials [73].

3.7 The finite element method (FEM)

The finite element method (FEM) is a numerical technique used to solve partial differential equations (PDEs) and analyze complex engineering and scientific problems. It is widely employed in various fields, including structural analysis, fluid dynamics, electromagnetics, and heat transfer.

At its core, the FEM divides a complex problem domain into smaller, simpler regions called finite elements.[74] These elements are geometrically connected to form a mesh that discretizes the domain. The PDEs governing the problem are then approximated within each element using polynomial interpolation functions. By applying boundary conditions and assembling the element equations, a global system of equations is generated, which can be solved to obtain approximate solutions for the problem variables.

3.8 FEM and EEG

Moving on to the application of the finite element method in Electroencephalography (EEG) source analysis, EEG is a non-invasive neuroimaging technique that measures the electrical activity of the brain through electrodes placed on the scalp. Source analysis aims to estimate the underlying neural activity responsible for the observed EEG signals.

The finite element method can be utilized in EEG source analysis to model the electrical conduction within the head. By creating a realistic head model, which includes the scalp, skull, and brain compartments, the FEM can simulate the propagation of electrical currents and their interaction with the brain tissues[75]. This enables the estimation of the location and strength of the neural sources generating the observed EEG signals.

In EEG source analysis, the FEM is typically used in conjunction with inverse methods, such as the distributed source model or the equivalent current dipole model, to estimate the neural activity based on the measured EEG data. The FEM helps in accurately modeling the forward problem, i.e., the propagation of electrical currents, which is a crucial step in solving the inverse problem of estimating the neural sources.

3.9 Inverse Solutions

The EEG inverse problem is considered ill-posed due to two main reasons. Firstly, the solution is non-unique because there are many possible output voltages that can be obtained for a given input ($p \gg N$, for N electrodes and p dipoles). Secondly, the solution is unstable, meaning it is highly sensitive to even small changes in the noisy data. To address this issue, several methods have been developed.

In the case of the EEG inverse problem, a dipole is characterized by six parameters: three spatial coordinates (x, y, z) and three components of the dipole moment (orientation angles θ, ϕ, and strength d). However, it is possible to reduce these parameters by imposing constraints on the source, as explained below.

Depending on the specific assumptions made regarding the number of dipoles and the fixed or known parameters such as dipole positions, magnitudes, and orientations, there exist various mathematical models. In the literature [76], several models have been proposed. These include:

- A model with a single dipole that has time-varying and unknown position, orientation, and magnitude.
- A model with a fixed number of dipoles where the positions and orientations are unknown but fixed, while the amplitudes vary.
- A model with known fixed dipole positions but varying orientations and amplitudes.
- A model with a variable number of dipoles, typically one dipole per grid point, while imposing a set of constraints.

In addition to these models, dipole moment constraints are sometimes necessary to narrow down the search space for meaningful dipole sources. Rodriguez-Rivera et al. [77] discuss four different dipole models that involve distinct dipole moment constraints.These are (i) constant unknown dipole moment; (ii) fixed known dipole moment orientation and variable moment magnitude; (iii) fixed unknown dipole moment orientation, variable moment magnitude; (iv) variable dipole moment orientation and magnitude.

There are two primary ways to solve the inverse problem: non-parametric and parametric methods. Non-parametric optimization methods are also known as Distributed Source Models, Distributed Inverse Solutions (DIS), or Imaging methods. These models involve distributing multiple dipole sources throughout the entire brain volume or cortical surface, with fixed locations and potentially fixed orientations. On the other hand, parametric methods seek to identify the optimal position and orientation of a dipole. These parametric models can involve either a single dipole in a spherical head model or multiple dipoles in a realistic head model. In this thesis, only non-parametric techniques have been utilized, aiming to estimate the moment of dipoles within a predetermined source space. This approach results in a linear problem.

3.9.1 Bayesian framework

Bayesian methods offer the flexibility to estimate not only a single "best" solution but also a probability distribution of solutions. This means that instead of obtaining a single optimal solution, Bayesian approaches allow for capturing the uncertainty and variability in the possible solutions.[78]

In general, this technique consists in finding an estimator $\hat{\mathbf{x}}$ of $\mathbf{x}$ that maximizes the posterior distribution of x given the measurements $\mathbf{y}$. This estimator can be written as

$$\hat{\mathbf{x}} = \max_{x}[p(\mathbf{x}|\mathbf{y})] \tag{3.38}$$

where $p(\mathbf{x}|\mathbf{y})$ denotes the conditional probability density of x given the measurements y. This estimator is the most probable one with regards to measurements and a priori considerations. According to Bayes' law,

$$p(\mathbf{x}|\mathbf{y}) = \frac{p(\mathbf{y}|\mathbf{x})p(\mathbf{x})}{p(\mathbf{y})} \tag{3.39}$$

Both the measurements recorded from the EEG channel, denoted as $X \in \mathbb{R}^{q\times t}$, where q is the number of EEG channels while p is the number of dipoles, and the the electrical current of each dipole$S \in \mathbb{R}^{q\times t}$ are considered as random variables. The

noise present in the system is modeled as a zero-mean Gaussian random variable $\mathbf{n} \sim \mathcal{N}(0, \sigma^2 \mathbf{I}_q)$ [69] Therefore,

3.9.2 Minimum Norm Estimate (MNE)

A common approach to address the inverse problem involves representing the current distribution using a small set of parameters. Nonetheless, it can be challenging to find a source model that is both sufficiently restrictive to ensure a unique solution and capable of accurately describing the fundamental characteristics of the current distribution. A commonly employed model, which is suitable for interpreting basic neuromagnetic field patterns, is the current dipole (Williamson and Kaufman, 1981). When using the dipole model to locate brain activity, it assumes that the source current is concentrated within a small region (or multiple separate regions in multi-dipole models). However, if these assumptions are not valid, it can lead to misleading outcomes. [22]

According to [22] the minimum-norm estimates (MNEs) are presented as the most accurate estimates for the distribution of source currents, particularly when limited prior information about the source is available. When there are no assumptions made about discrete current elements, the estimates yield continuous current distributions.

Chapter 4

Deep Learning

Deep learning is a subfield of machine learning that focuses on training artificial neural networks with multiple layers to learn and extract hierarchical representations of data. It is inspired by the structure and functioning of the human brain, specifically the interconnected network of neurons. [79]

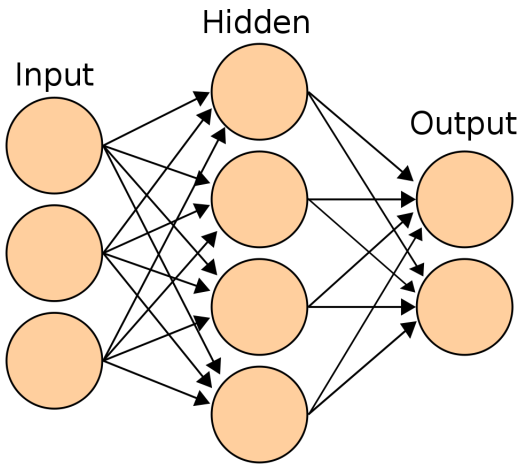

FIGURE 4.1: An artificial neural network is an interconnected group of nodes, inspired by a simplification of neurons in a brain. Here, each node, depicted as a circular shape, represents an artificial neuron and the connections between nodes, indicated by arrows, represent the flow of information from the output of one artificial neuron to the input of another.

In deep learning, neural networks with multiple hidden layers, often referred to as deep neural networks, are capable of learning complex patterns and relationships from vast amounts of data. Deep learning models employ a hierarchical representation of data, where each layer learns and extracts higher-level features based on the features learned by the preceding layers. [80]

One of the key advantages of deep learning is its ability to automatically learn feature representations directly from raw data, eliminating the need for manual feature engineering. Deep learning models can handle various types of data, including images, text, speech, and sequences, and have achieved state-of-the-art performance in many domains, such as computer vision, natural language processing, speech recognition, and recommendation systems. [81, 79].

Deep learning algorithms, such as Convolutional Neural Networks (CNNs) and Recurrent Neural Networks (RNNs), use large-scale datasets and powerful computational resources to iteratively train the network parameters. The training process typically involves optimizing a loss function through backpropagation, adjusting the weights and biases of the network to minimize the prediction errors. [82].

4.1 Neurons in deep learning

4.1.1 Biological neuron

The human brain relies on the coordination of groups of neurons to carry out various tasks essential for our daily functioning. Geoffrey Hinton, a prominent researcher in neural networks, posed an important question: Can we develop computer algorithms that emulate the behavior of brain neurons? The goal was to replicate the brain's structure in the hope of harnessing its capabilities.

To accomplish this, researchers closely examined how neurons operate in the brain and discovered a crucial insight: an individual neuron alone is ineffective. The true power lies in interconnected networks of neurons, since neurons function by receiving and sending signals.

To be more precise, a neuron receives signals through its dendrites and transmits them along its axon. The dendrites of one neuron are linked to the axon of another neuron through specialized connections known as synapses. These synapses have been generalized and adopted in the field of deep learning as a fundamental concept.

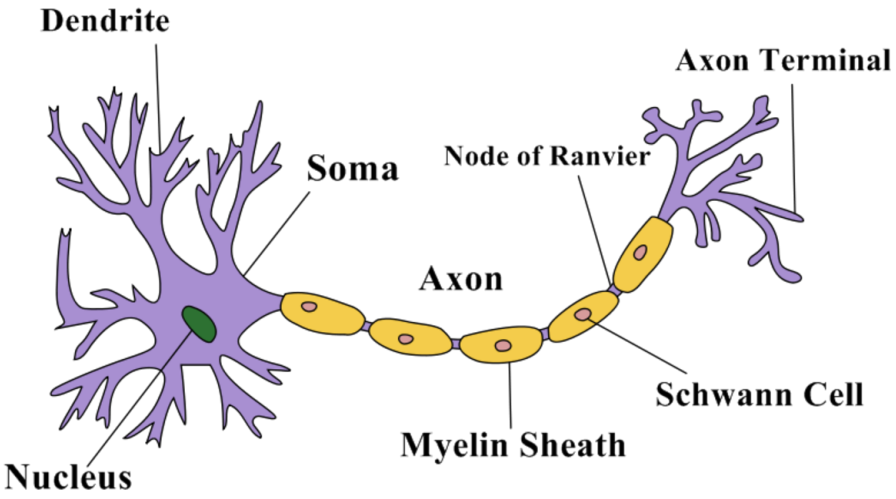

FIGURE 4.2: Diagram of a neuron in the human brain

4.1.2 Artificial neuron

An artificial neuron, also known as a node or unit, is the fundamental building block of a neural network. It is inspired by the structure and functioning of biological neurons in the human brain. Artificial neurons are designed to process and transmit information in a neural network, enabling the network to perform complex tasks such as pattern recognition, decision-making, and learning.

An artificial neuron typically takes multiple input signals, each multiplied by a corresponding weight, and then adds these weighted inputs together. The neuron also includes a bias term that acts as an offset to the sum of the weighted inputs. The result of this summation is passed through an activation function, which introduces non-linearity to the neuron's output.

The mathematical representation of an artificial neuron can be described as follows:

- Inputs: Let's say there are n input signals represented as $x_1, x_2, ..., x_n$.
- Weights: Corresponding to each input signal, there are weights represented as $w_1, w_2, ..., w_n$.
- Bias: A bias term represented as b is added to the summation of weighted inputs.
- Summation: The weighted inputs and the bias term are added together to produce a weighted sum: $z = w_1 * x_1 + w_2 * x_2 + ... + w_n * x_n + b$.
- Activation Function: The weighted sum (z) is then passed through an activation function (often denoted as g(z)), which introduces non-linearity to the neuron's output. Common activation functions include the sigmoid, ReLU (Rectified Linear Unit), tanh (hyperbolic tangent), and more.
- Output: The output of the artificial neuron is the result of the activation function: $y = g(z)$.

The output of this artificial neuron then becomes an input to subsequent layers in the neural network, and the process is repeated throughout the network until the final output is obtained. By learning the appropriate weights and biases during the training process, neural networks can approximate complex functions and make predictions based on input data.

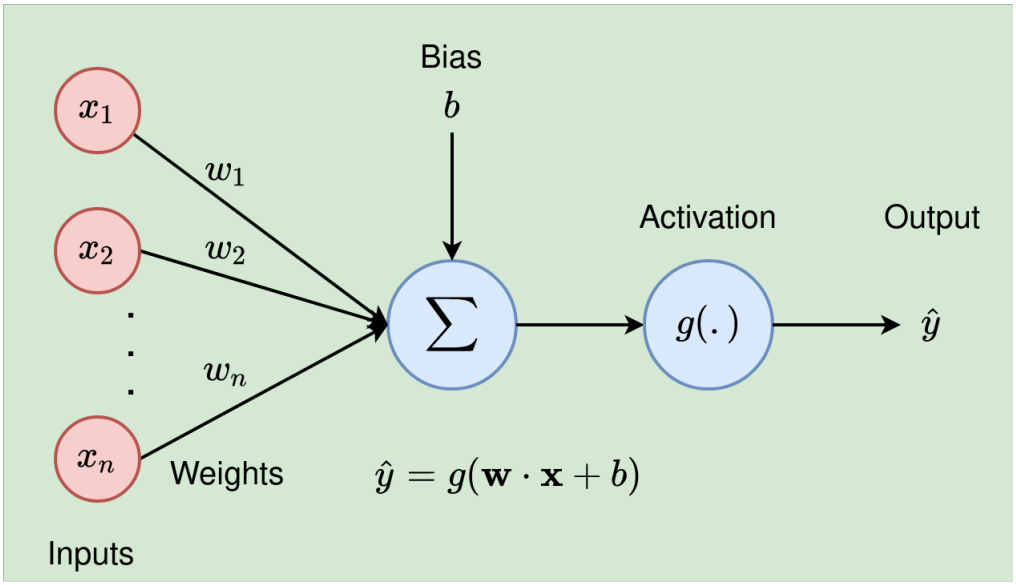

FIGURE 4.3: Diagram of an artificial neuron

4.2 Convolutional Neural Networks (CNNs)

A Convolutional Neural Network (CNN) is a deep learning algorithm specifically designed for processing and analyzing visual data [83]. More specifically, it is a series of interconnected layers of neurons where each layer applies a differentiable function to transform one volume of activations into another.

The CNN architecture primarily consists of three types of layers:

- convolutional layers
- fully-connected layers
- pooling layers.

The transformation process within the CNN involves converting the input image volume into an output volume by passing it through multiple hidden layers. Each hidden layer consists of a group of neurons that perform a linear operation on the input. In the case of convolutional layers, this operation involves convolution, while fully-connected layers utilize dot-product calculations. Following the linear transformation, a non-linear activation function, such as ReLU or sigmoid, may be applied to introduce non-linearity to the output.

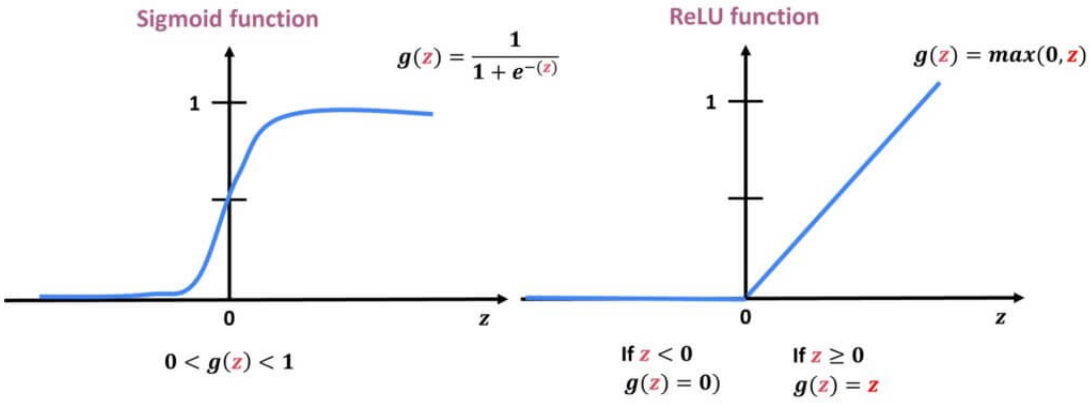

FIGURE 4.4: ReLU and sigmoid activation functions

The input and output of each hidden layer are sets of arrays called feature maps. Each layer can contain certain parameters and extra hyperparameters. Unlike a standard neural network, the CNN expects the input data to possess spatial characteristics, such as correlations in neighboring pixels in an image. The term "width of the network" is used to describe the number of filters a layer has, while the term "depth of the network" refers to the number of layers.

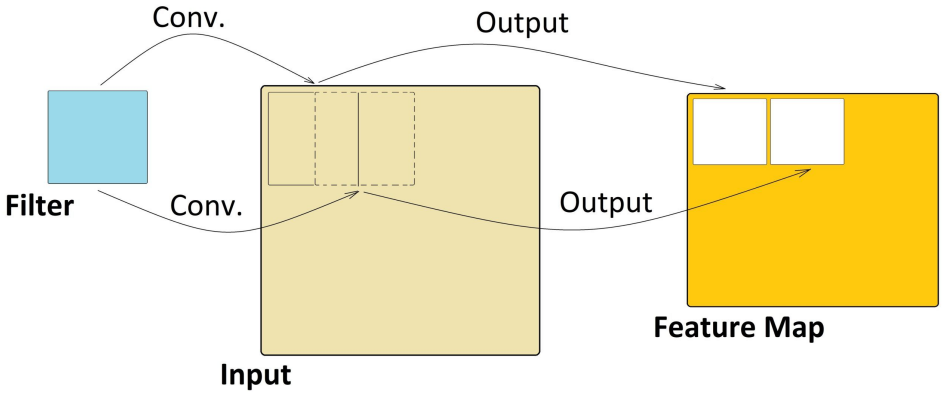

4.2.1 Convolutional layer

Convolutional layers serve as the fundamental building blocks of Convolutional Neural Networks as they carry out the computationally heavy work. More specifically, a convolutional layer consists of a set of filters with learnable parameters and each filter has relatively small dimensions in terms of width and height, but it covers the entire depth of the input feature map. So for example, when the input image is RGB, the first filter of a convolutional layer will have dimensions of $w \times h \times \times 3$

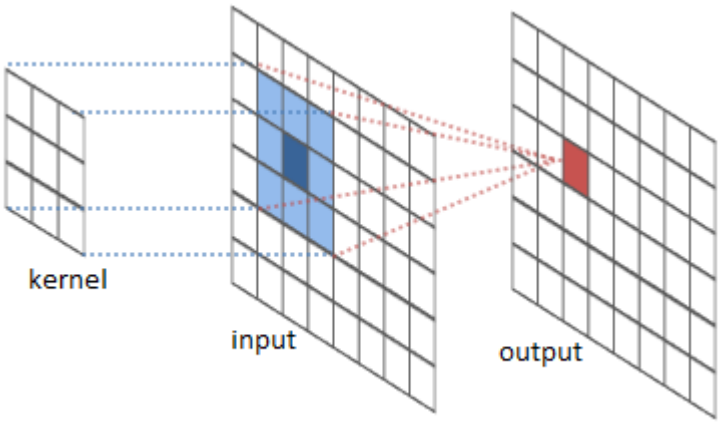

FIGURE 4.5: Convolution operation

as shown in picture **??**, when performing a convolution operation on an image (input) using a filter (also known as a kernel), the process involves calculating a new output pixel value (shown in red) by taking a weighted sum of the original pixel's value (shown in dark blue) and its neighboring pixels' values (shown in blue). The filter's values determine the specific weights used for the summation (weighted sum of the pixel), and this sliding operation is applied across the entire image, producing the final convolved output.

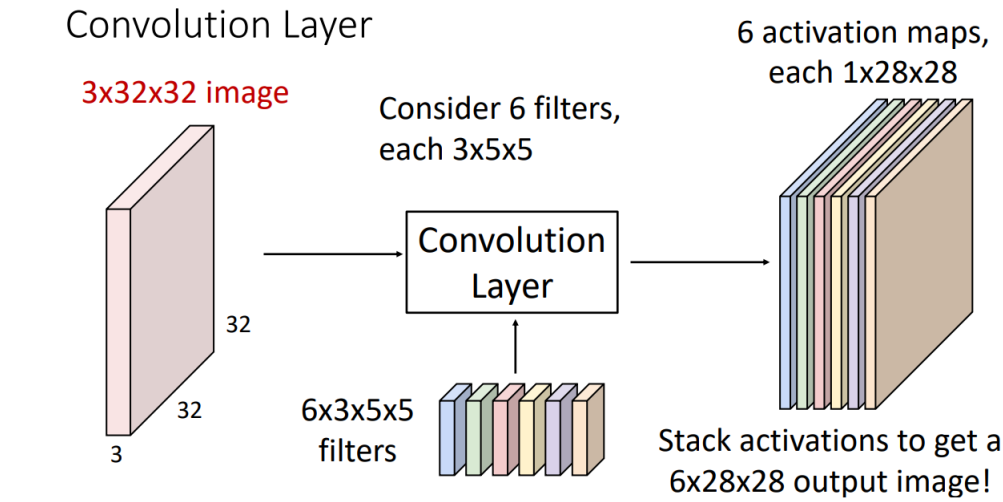

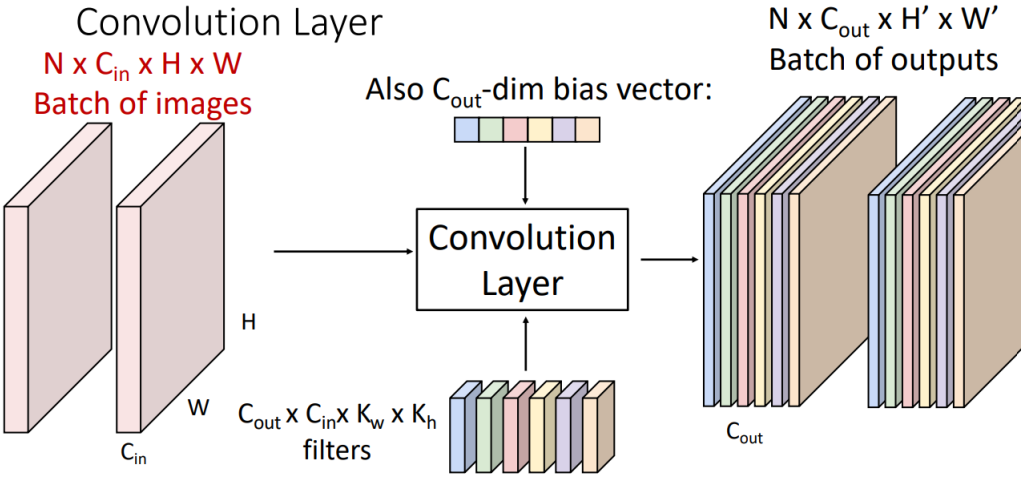

The above images are taken from: https://web.eecs.umich.edu/~justincj/slides/eecs498/FA2020/598_FA2020_lecture07.pdf

4.3 Common CNN Architectures

Some common CNN architectures that have made significant contributions to the field of the deep learning include:

- AlexNet
- VGG
- ResNet

4.3.1 AlexNet

AlexNet [8] is a groundbreaking convolutional neural network (CNN) architecture that had a significant impact on the field of deep learning and computer vision. It won the ImageNet Large Scale Visual Recognition Challenge (ILSVRC) in 2012,

which involves classifying millions of high-resolution images into thousands of different categories.

AlexNet [8] utilized a deep architecture which composes of eight layers, including five convolutional layers followed by three fully connected layers. In between these layers there are also ReLu and pooling layers.The Rectified Linear Unit (ReLU) activation function significantly reduces training time when compared to using sigmoid and tanh activations. The success of AlexNet popularized the ReLU as the preferred activation function for training deep Convolutional Neural Networks (CNNs). Max-pooling layers are applied after some of the convolutional layers. These layers reduce the spatial dimensions of the feature maps and introduce translation invariance, making the network more robust to variations in object position within the input images.Additionally, to mitigate the issue of overfitting, Krizhevsky et al. [8] incorporated dropout layers into their model, a technique introduced by Srivastava et al. in 2014 [84].For the training of AlexNet, batch Stochastic Gradient Descent (SGD) was used, along with specific settings for parameters like momentum and weight decay. Additionally, throughout the training process, data augmentation methods like image translations, horizontal flips, and patch extractions were also applied. As shown in (4.6), AlexNet was divided into two parts as it was unfeasible for it to fit within the memory of a single GPU. This division had additional benefits: the filters within the second, fourth, and fifth convolutional layers take as input preceding feature maps from the same GPU. This design choice reduced the overall number of learnable parameters within the network, which yielded favorable performance outcomes.

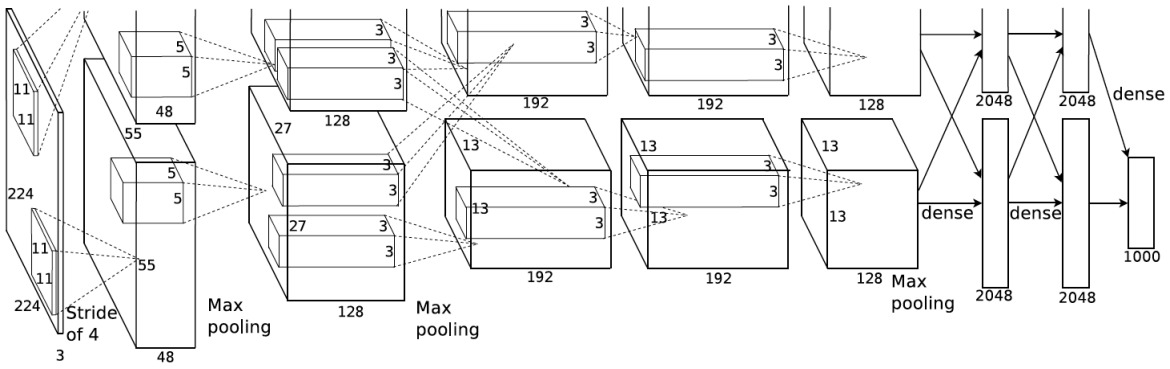

FIGURE 4.6: Illustration of the AlexNet Architecture, which is shown to be split in two part, each operating in a different GPU.

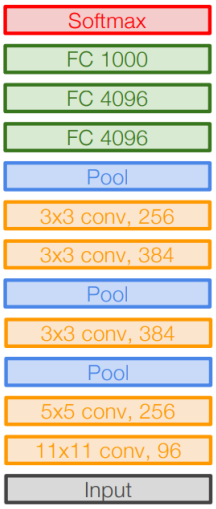

FIGURE 4.7: Layer representation of Alex net

4.3.2 VGG

The VGG (Visual Geometry Group) neural network is a deep convolutional neural network known for its simplicity, depth and uniform architecture. Simonyan and Zisserman in [9] explored how the depth of the neural network impacts its accuracy when when dealing with large-scale image recognition tasks. A thorough evaluation of networks of increasing depth using an architecture of 3x3 convolution filters showed that significant improvements on the prior-art configurations can be achieved by pushing the depth to 16–19 weight layers. [9] The most commonly used architecture out of these is VGG16 which has 16 convolutional and fully-connected layers and about 138M parameters. The architecture of VGG16 is shown in figure (4.8) below:

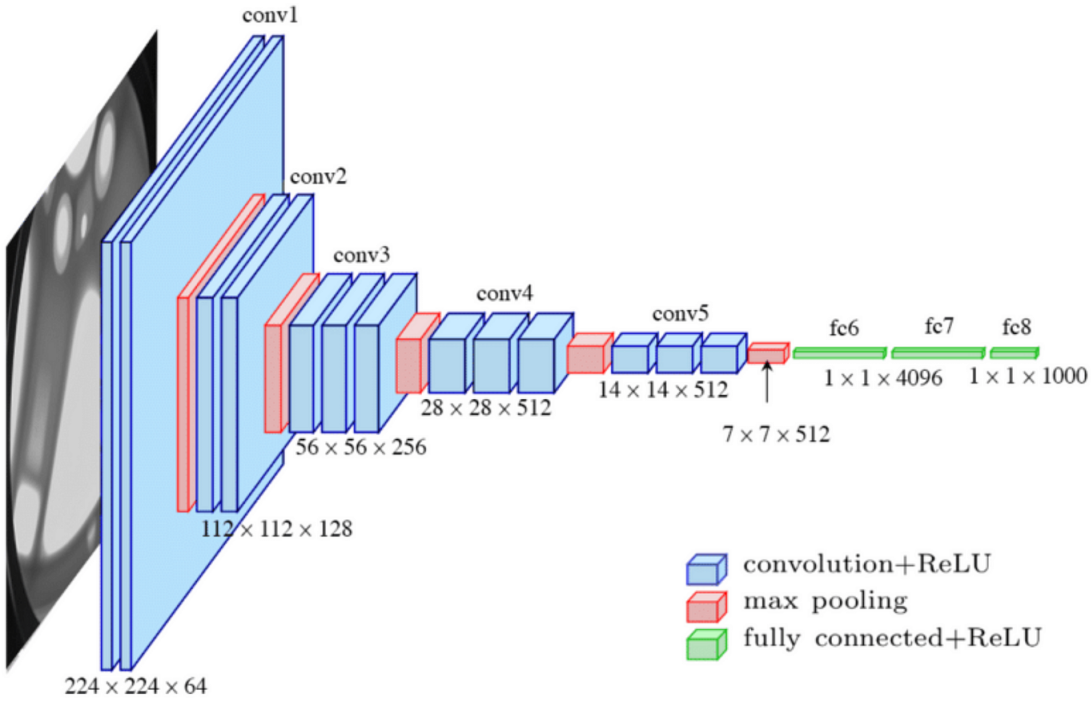

FIGURE 4.8: Illustration of the VGG16 architecture.

VGG16 is composed of:

a 13 convolutional layers, shown in blue

b 5 pooling layers that perform 2 x 2 max - pooling

c 3 fully connected layers

The activation function that is used (non-linearity) is the Rectified Linear Unit (ReLU) one and it is applied after both each convolutional and each fully connected layer.

4.3.3 ResNet

As illustrated in figure (4.9), residual networks consist of a stack of many residual blocks, where each block has two 3x3 convolutions. The network is made up of stages (depicted in different colors in (4.9) and at the first block of each stage the resolution is halved using a stride-2 convolution while the number of channels is doubled. At the top of the network, there's only one linear layer which follows a global average pooling layer.

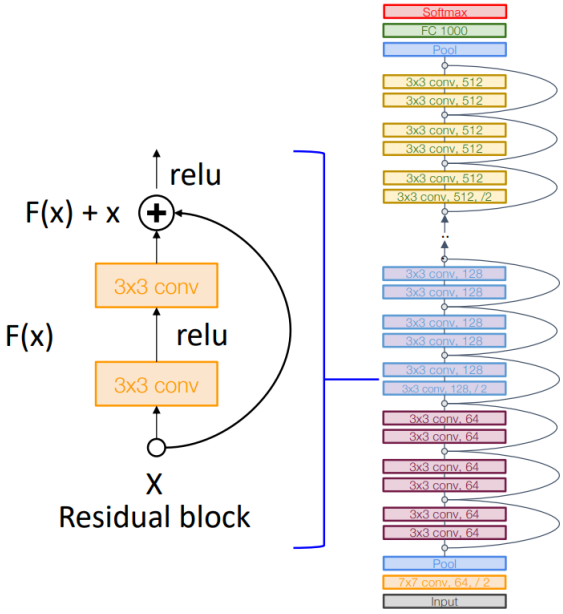

FIGURE 4.9: The above images are taken from: https://web.eecs.umich.edu/~justincj/slides/eecs498/WI2022/598_WI2022_lecture08.pdf

ResNet-18 and ResNet-34 utilize the "Basic" residual block shown in figure (4.9). However, ResNet-50, ResNet-101 and ResNet-152 utilize the "Bottleneck" building block, which introduces more layers in the network but less computational cost:

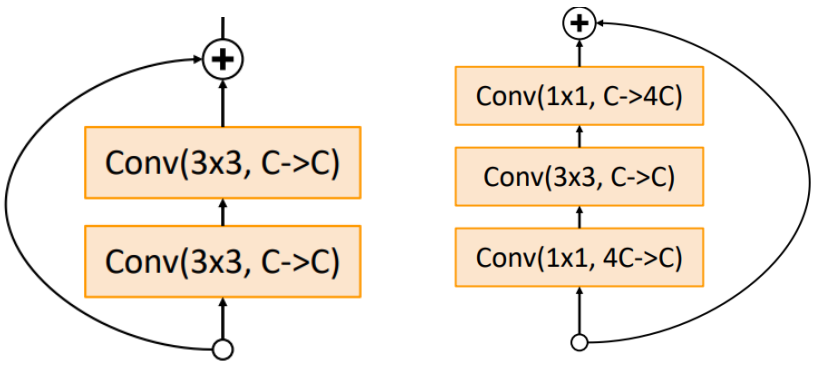

(A) Basic Residual Block (B) Bottleneck Residual Block

FIGURE 4.10: Total FLOPs in residual block are $18HWC^2$ whereas total FLOPs in bottleneck block are $17HWC^2$ - pictures taken from https://web.eecs.umich.edu/~justincj/slides/eecs498/WI2022/598_WI2022_lecture08.pdf

Chapter 5

Method

5.1 Modeling for the solution of the forward problem

For the solution of the EEG Forward problem, the techniques that are most commonly used are the Bounded Element Methods (BEM) **??**, the Finite Element Methods (FEM) [85] or the Finite Difference Methods (FDM) [86]. In this thesis, the method that was employed is the Finite Element Method (FEM) due to its remarkable flexibility in accurately simulating the propagation of electromagnetic fields within complex and challenging head volume conductors, particularly those that are inhomogeneous and anisotropic, such as the human head. [87, 88]

In this thesis, the source space consists of 50,460 dipoles and a set of 74 electrodes, while also following the 10-10 system configuration and a level of precision at the millimeter scale. An accurate head volume conductor model is also crucial for capturing both the geometric and dielectric characteristics of the head. Precise estimation of these properties is essential for obtaining reliable solutions in both forward and inverse analyses. However, achieving this accuracy is challenging due to the presence of numerous head tissues with varying conductivities and the differences in conductivity observed among individuals. Notably, the human skull's conductivity is particularly variable and requires careful consideration in the modeling process.

In this tesis, a six-compartment head model (6C) has been utilized, which consists of:

- skin
- skull compacta
- Cerebrospinal fluid (CSF)
- skull spongiosa
- grey matter
- white matter

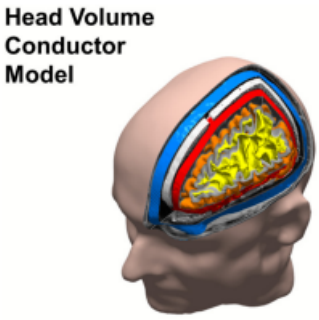

FIGURE 5.1: Main ingredients of the six-compartment head model: skin (human light skin color), skull compacta (blue), cerebrospinal fluid (red), skull spongiosa (gray), grey matter (orange), white matter (yellow)

The head tissue conductivities that were used for one of the head models in this thesis were 0.43 S/m for scalp skin, 0.0031 S/m for skull compacta and 1.79 S/m for cerebrospinal fluid, whereas for skull spongiosa it was set at 0.01116 S/m. It should also be noted that for each participant involved in this thesis, a source space with a resolution of 2 mm was established at the center of the gray matter compartment, without imposing any limitations on source orientations (without normal constraints). This approach ensured that all sources were situated within the gray matter and maintained a sufficient distance from neighboring tissue compartments, in order to ensure the Verant condition, according to which, for each source node, the nearest finite element node should exclusively belong to elements categorized as gray matter. This condition must be met to prevent numerical issues and unrealistic source representation when employing the chosen Venant dipole modeling method. [87, 88]

5.2 Solution of the forward problem

The first step for solving the forward problem requires the creation of a realistic head volume conductivity model, which is essential for interpreting how the brain's electrical signals from the source are being transmitted to electrodes on the scalp. The forward problem is addressed by calculating the leadfield matrix, when both the neural sources in the brain and the potentials recorded at EEG electrodes are known by making use of equation (5.2) :

$$\mathbf{X} = \mathbf{LS}$$

In this thesis, we make use of the Finite Element Method in order to compute the leadfield matrix, although it comes along with a higher computational cost, because of its high flexibility in accurately simulating the propagation of electromagnetic fields within complex inhomogeneous and anisotropic conductors, such as the human head.

The EEG leadfield matrix is calculated using Duneuro [89] while employing the conventional finite element method (CG-FEM) [85], and adopting the Venant source model with the transfer matrix approach [90].The Venant direct source modeling approach was chosen due to notable numerical accuracy and efficient computational performance especially when it is combined with EEG and MEG transfer matrices

for EEG and MEG and an algebraic multigrid preconditioned conjugate gradient (AMG-CG) solver. When using FEM, a larger number of elements is necessary in order to model intricate geometries within the modeled volume, while the use of sparse matrices contributes to notable reductions in computational costs. By utilizing efficient solvers like parallel algebraic multigrid preconditioned conjugate gradient method and especially fast FEM transfer matrix approaches, it is possible to solve the EEG forward problem across numerous head models with millions of elements [91].

Within the framework of FEM, the volume of the head is modeled using three dimesional elements like hexahedra or tetrahedra. The benefit of hexahedra is that its easier and faster to acquire the mesh out of the labeled MRI. In the case of hexahedral meshes, it is feasible to directly transform the voxels within the labeled MRI volume into mesh elements. However, unlike tetrahedral meshes, this direct conversion is not applicable, and additional steps are required to refine the segmented model, ensuring that tissue compartments do not intersect one another. Employing hexahedral meshes has been demonstrated to yield edges that are not smoothly contoured and less realistic, a phenomenon commonly referred to as the "staircase effect." This issue is alleviated by repositioning the nodes along the material interfaces [91]. This approach was evaluated in EEG source analysis with multi-layer sphere models, showing major error reductions compared to regular hexahedral approaches [85]

5.3 Simulation of the training data

The aim of the CNN that is proposed in this thesis, is to solve the EEG inverse problem, i.e. to predict the source regions inside the brain (dipoles) where electrical activity occurred given the measurements of the scalp electrodes.

For the training of our CNN, a large number of simulated data samples is used, which consists of EEG topographies and their respective ground truth source inside the brain. The neural network that is proposed in this thesis, performs source localization for up to three sources inside the brain. When generating the data, a random number of sources is selected, which can be either one, two, or three. Then, depending on the selected number of sources, the respective number of dipoles are randomly being selected from the source space and then a region growing approach is applied as described in [3]. Briefly, after a random seed dipole is selected, all its neighboring dipoles, up to a specific radius r, are recursively included but with attenuated moments depending on their distance to the seed dipole, which was assigned a dipole moment between five and ten Nano-Ampere Meter (nAm). The attenuation of the neighboring dipoles followed a Gaussian distribution with a mean of the seeding dipole moment and a standard deviation of half the radius of the dipole cluster, yielding smooth source patches [3].

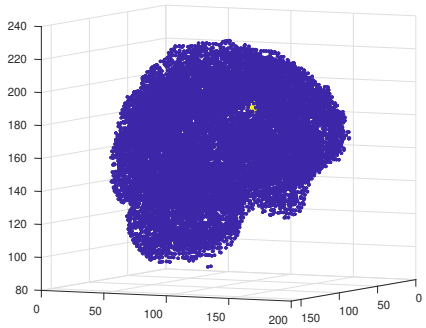

(A) step 1 - seed dipole

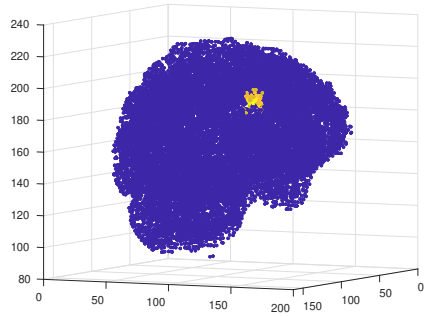

(B) step 2

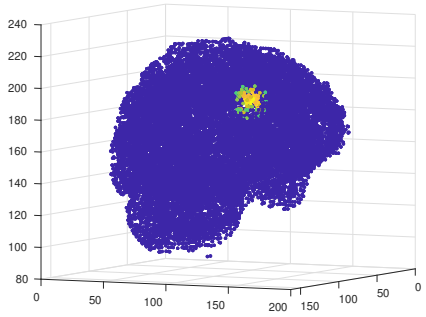

(C) step 3

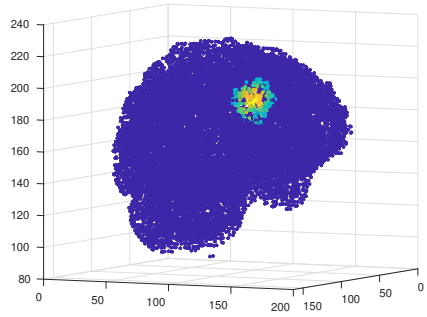

(D) step 4

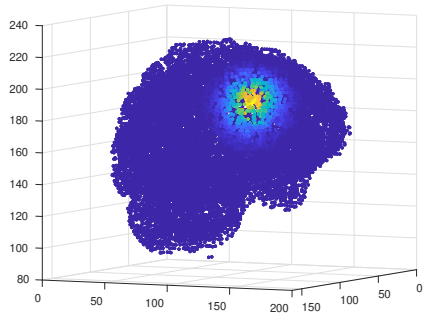

(E) final result

FIGURE 5.2: Visualization of the source simulation steps

In terms of mathematical representation for this problem, for $p = 50,460$ dipoles and $q = 74$ EEG electrodes and for each time point:

$$\mathbf{X} = \mathbf{LS} \tag{5.1}$$

where, $X \in \mathbb{R}^{q \times t}$ is the estimated EEG channel measurements over time t, $L \in \mathbb{R}^{q \times p}$ is the leadfield matrix that has been obtained by solving the forward problem and $S \in \mathbb{R}^{q \times t}$ represents the electrical current of each dipole over time.

For a specific time t, $S \in \mathbb{R}^{50,460}$ and it represents the simulated electrical activation shown in figure 5.2e. In order to create the simulated data, S is projected on the leadfield matrix L, and the result yields the values of the 74 EEG electrodes $\mathbf{X} \in \mathbb{R}^{74}$. Here, since the CNN has been trained for $N = 3$ different anatomies, the training data has been generated with N different leadfield matrices. More specifically, 300,000 data samples has been used, 100,000 for each anatomy.

To make the training data more realistic, Gaussian white noise $\mathbf{n} \sim \mathcal{N}(0, \sigma^2 \mathbf{I}_q)$ was added:

$$\mathbf{X} = \mathbf{LS} + \mathbf{n} \tag{5.2}$$

To be more precise, the equaion for the SNR is the following:

$$SNR = 10 \ log\left(\frac{P_{signal}}{P_{noise}}\right) \tag{5.3}$$

where P_{signal} is the power of the simulated electrical activation and P_{noise} is the power of the additive Gaussian noise
The aforementioned simulated process randomly selects a value from each of the following settings:

- number of sources: 1-3
- source extent: 5-30 mm
- amplitudes 5-10 nAm
- snr $\in \{-10, -5, 0, 5, 10, 15, 20, 25, 30\}$

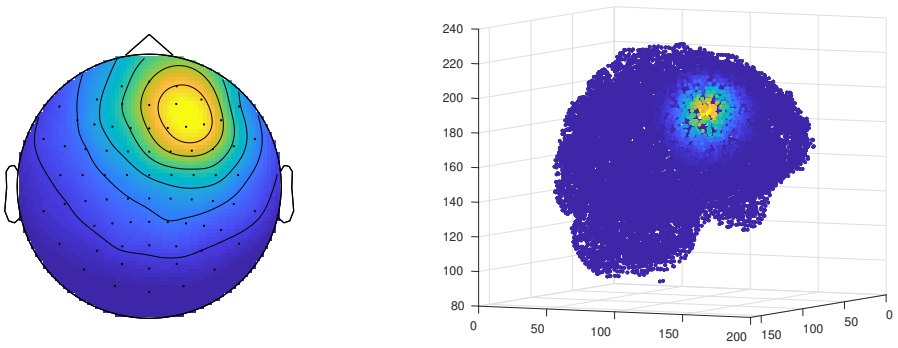

(A) Simulated topography (B) Simulated source

FIGURE 5.3: Simulated source and its corresponding topography

Finally, in Figure 5.3 we visualize a topography with its respective source activation. The EEG topography is obtained by employing a library from FieldTrip, which is a MATLAB-toolbox for the analysis of MEG, EEG, and other electrophysiological data, which is freely available from `http://www.ru.nl/neuroimaging/fieldtrip` under the GNU public license. [92]

5.3.1 Training data

For the training of the neural network, 300,000 samples were created, 100,000 from each anatomy. For every sample, the number of sources (1-3) was selected randomly and the amplitude ranges from 5 to 10 nAm whereas the source extend varies from 5 to 30 mm.

5.3.2 Evaluation (Testing) data

For the evaluation of the neural network, for each sample, the number of sources (1-3) was selected randomly and the amplitude ranges from 5 to 10 nAm whereas

the source extend varies from 5 to 15 mm. One major difference from the training data is is the SNR which ranges from $-5dB$ to $-25dB$

The picture below illustrates the splitting of the dataset for training, testing, and validation:

5.4 Visualization of simulated data

We now visualize electrical activations with 1 to 3 seed dipoles sources.

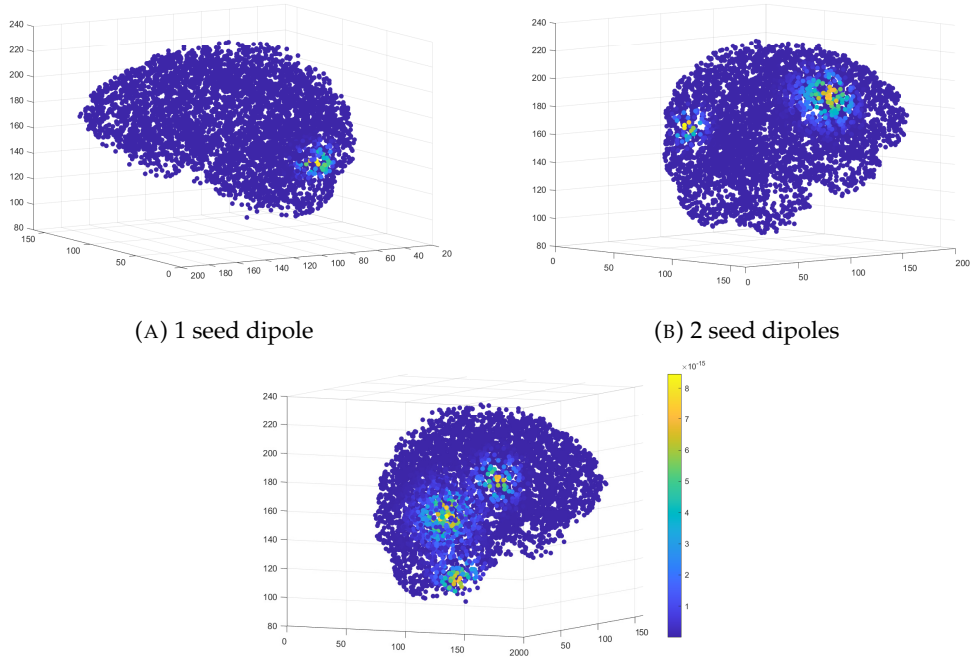

(A) 1 seed dipole

(B) 2 seed dipoles

(C) 3 seed dipoles

FIGURE 5.4: Simulated sources with 1 to 3 dipoles

In Figure 5.4, we can observe the number of clusters for each electrical activation. For instance, in Figure 5.4(C), we see three clusters, each corresponding to one seed dipole. Our deep learning model will be trained to predict the amplitude of each dipole in the source space. Therefore, the model will be capable of localizing EEG signals associated with more than one seed dipole.

5.5 Solution of the Inverse problem

5.5.1 CNN

Convolutional Neural Networks (CNNs) and EEG source localization are two distinct but related concepts in the field of neuroscience and machine learning. CNNs are a class of deep neural networks designed primarily for processing grid-like data, such as images and time-series data. This is the reason why the input of the proposed Neural Network is a topography of the EEG-signal rather than the EGG signal itself. CNNs are characterized by the use of convolutional layers, which specialize in extracting features from input data by applying convolution operations and they

can play a valuable role in EEG inverse problems by extracting informative features from EEG data and aiding in spatial and temporal analysis.

CNN Architecture

The proposed CNN solved the EEG inverse problem for 1-3 sources and for different anatomies. It was developed using Python and Pytorch and it's architecture is inspired by the VGG Neural network [9]. More specifically, the input of the CNN is an EEG topography picture, 67x67, as shown in 5.4a and the output consists of 5046 values that make up the source space. It has 138M parameters and mathematicaly it can be described as:

$$\Phi : \mathbb{R}^{67x67} \rightarrow \mathbb{R}^{5046} \tag{5.4}$$

The neural network consists of:

(a) 6 convolutional layers, each followed by batch normalization and then a ReLu

(b) 2 pooling layers that perform 2 x 2 max - pooling after the first two ReLus

(c) 1 global average pooling layer

(d) 2 fully connected layers on top of the network

Batch normalization is an effective technique that consistently accelerates the convergence of deep networks. During model training, it continuously adjusts the intermediate output of the network by utilizing the mean and standard deviation of the minibatch, so that the values of the intermediate output in each layer throughout the neural network are more stable [93]. Everytime a pooling layer is applied, the width and height of the image gets divided in half. For example, initially, the input is a picture 1x67x67, which means that the number of channels is equal to 1 (grayscale image), the width is 67 and the height is also 67. After the first convolutional layer, since the number of channels (also known as filters) is 128 and the filter we use is 3x3, with padding 1, we get 128 activation maps, each 1x67x67. After the max pooling, the spatial dimensions (height and width) of the input topography are halved. In order to maintain sufficient height and width we only use 2 max pooling layers.

The global average pooling that takes place just before the fully connected layers serves the purpose of converting the data into a 1x4096 vector which will be fed into the following fully connected layers. Since we have downsampled the source space to 5046 dipoles, we set the output of the last fully connected layer of the CNN to be 5046.

To sum up, the proposed CNN performs EEG source analysis for 1-3 sources and for different anatomies while taking as input a 67x67 EEG topography and outputting 5046 values that correspond to the source space of the brain.

5.5.2 ResNet

Like the preposed CNN, ResNet also solves the EEG inverse problem for 1-3 sources and for different anatomies and is was developed using Pytorch's pre-trained resnet models but with the addition of a fully connected last layer which outputs 5046

values so as to match the source space which is the desired output. After running experiments with resnet18, resnet50, resnet101 and resnet152, the neural network that performs best is

5.5.3 Training

We train our models on the simulated dataset (see Chapter 5.3) with 300K source activations and their corresponding topographies. We use the Mean Squared Error as the loss function as the model predicts the amplitude for each dipole in the source space. Furthermore, for a fair comparison, we train all of our models with the Adam optimizer [94] with a learning rate of 10^{-4} and a batch size of 32 samples.

5.6 Comparison with other studies

Our method is inspired by the pioneer studies [4, 6, 3, 5]. We now compare them in terms of forward modelling, input and output of the model.

Method	Forward Modelling	Input	Output
ESBN [6]	FEM [74]	EEG signal	Amplitude of each dipole
DeepMeg [4]	Brainstorm [95]	EEG signal	Location in the 3D-space
ConvDip [3]	BEM [68]	Topography	Amplitude of each dipole
feCNN [5]	FEM [74]	Topography	Location in the 3D-space
Ours	FEM [74]	Topography	Amplitude of each dipole

TABLE 5.1: Comparison of Deep Learning approaches

Our method is the only model that is trained with more than one anatomies. feCNN is the most closely related to our work. Our method differs from feCNN becuase our model is trained in 3 anatomies and with simulated electrical activations with more than one source dipoles.

Chapter 6

Evaluation

In this Chapter we evaluate the performance of our models and compare to state-of-the-art inverse algorithm sLORETA. We first use simulated data that are not part of the training set and thus we can observe the generalization ability of the models Additionally, we validate the performance of our networks on real data recorded during the doctoral of Dr. Antonakakis [91]. The key difference between the simulated and real data is that the real data are recorded with one source, while the simulated data have more activated sources.

6.1 Metrics

We use the localization error [96] as a metric to quantify EEG source localization performance. The localization error (LE) can be quantified as the Euclidean distance between the truly activated source r_{true} and the reconstructed peak source r_{peak} in the three-dimensional source space:

$$\text{LE} = ||r_{\text{true}} - r_{\text{peak}}||_2 \tag{6.1}$$

For source activation with more than one seed dipoles, we compute the average for each seed dipole.

The localization error requires knowledge of the location of the seed dipole (r_{true}) that generated the recorded activity from the EEG electrodes. In the case of simulated data, the seed dipole of the dipole cluster (see Section **??**) is known, allowing us to use the LE. On the other hand, with real-data we approximate the location of the seed dipole (see Section 6.5).

6.2 Evaluation with simulated data

We are now evaluating the performance of our models using simulated data. Specifically, for all three anatomies, we simulate data (as described in Section 5.3) by randomly selecting values from each of the following setting:

- number of sources: 1-3
- source extent: 5-30 mm
- amplitudes 5-10 nAm

We simulate 5000 samples for each snr $\in \{-5, 0, 5, 10, 15, 20, 25\}$.

6.2.1 Evaluation for various SNR levels

To assess localization accuracy in different realistic scenarios. We compared the performance of our models against the popular sLORETA [25] in the aforementioned snr levels for three anatomies. The results are shown in Figure. 6.1.

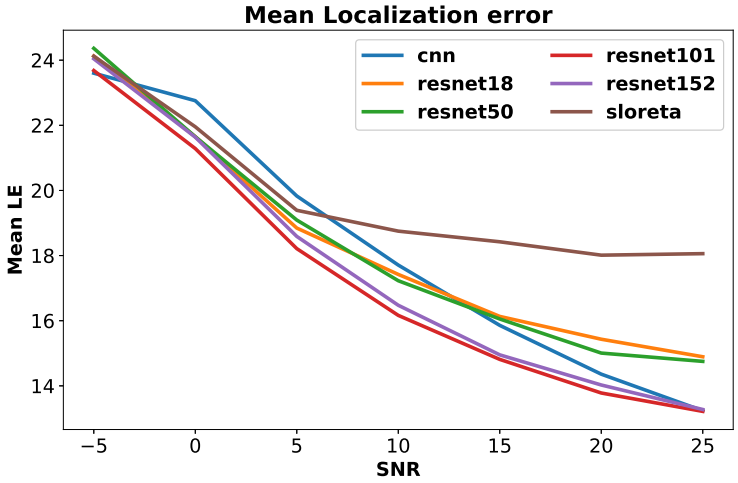

FIGURE 6.1: Localization Error for various SNR levels

From Figure 6.1, we observe that all of our models (cnn and resnets [10]) consistently outperform sLORETA [25]. Furthermore, sLORETA plateaus at 5 dB. We also observe that our models are not only capable of correctly localizing EEG data with more than one seed dipole but also capable of learning to localize them in three different brain anatomies.

6.2.2 Percentage of found sources

We now compare our models with sLORETA not in terms of localization error, but in terms of the percentage of found sources. Each sample from the simulated dataset has between 1 and 3 sources.

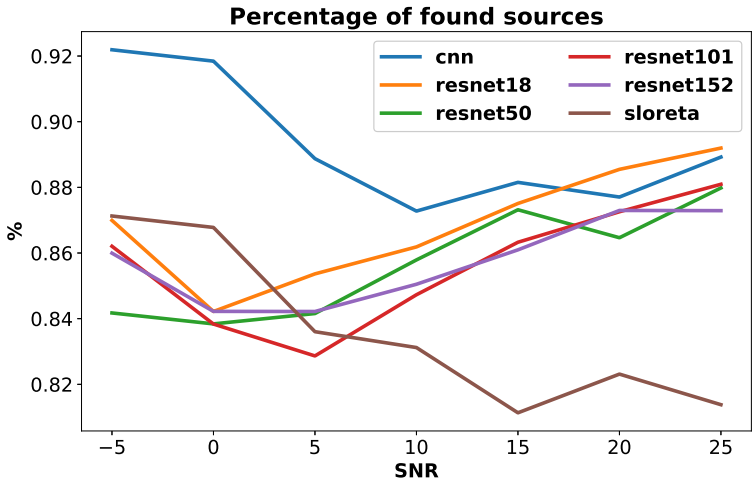

FIGURE 6.2: Percentage of found sources for various SNR levels

From Figure 6.2, we observe that sLORETA consistently finds less sources than all of our models. ResNet18 [10] outperforms all of our models at 25 dB of while the

custom CNN (blue line) is able to fine the most sources with higher noise levels (< -10 dB). Finally, the model ResNet18 [10] with only 18 million parameters is able to perform on par with the our VGG-like CNN (blue line) with 138 million parameters. This finding demonstrates the effectiveness of our training procedure.

For visualization purposes, we show in Figure. 6.3 a simulated topography for each signal-to-noise ratio. All the simulation have the same seed dipole and different SNR.

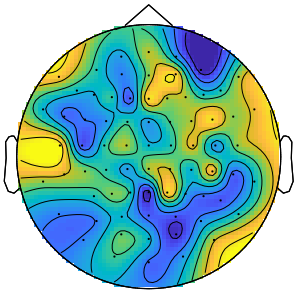

(A) SNR $= -10$dB

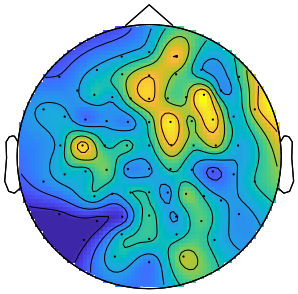

(B) SNR $= -5$dB

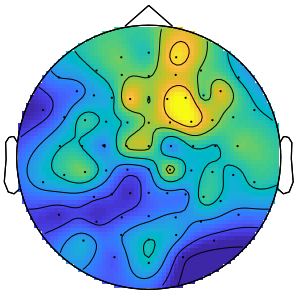

(C) SNR $= 0$dB

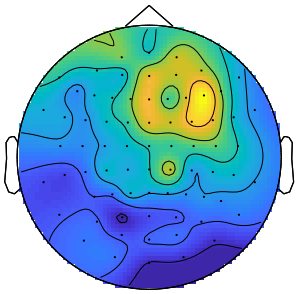

(D) SNR $= 5$dB

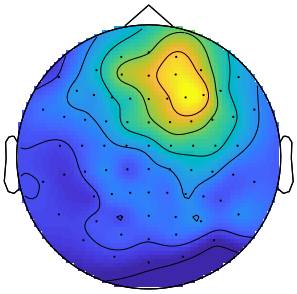

(E) SNR $= 10$dB

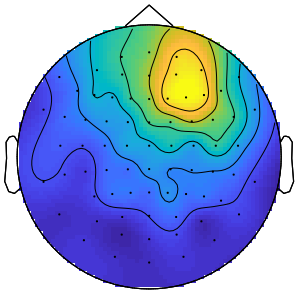

(F) SNR $= 15$dB

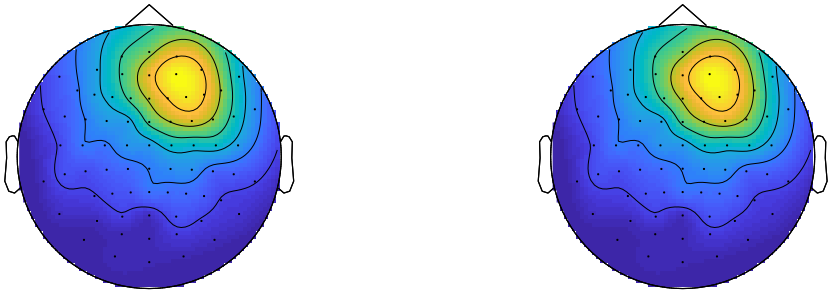

(G) SNR = 20dB (H) Without noise

FIGURE 6.3: Topographies for various SNR levels

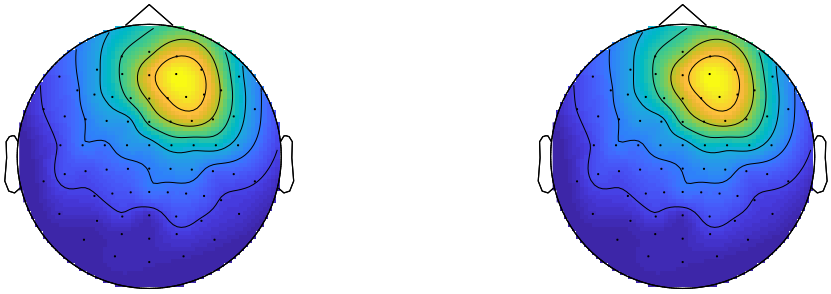

(I) SNR = 20dB (J) Without noise

FIGURE 6.3: Topographies for various SNR levels

We observe that our models are able to correctly localize EEG topographies for different anatomies and multiple sources even with low-quality images (< 0 dB)

6.2.3 Ablation analysis in the number of sources

Here, we provide an ablation analysis of our two best models, CNN and ResNet18, on the number of ground-truth sources. In particular, we report the localization error (see Eq. (6.1)) for various SNR levels and for a different number of ground-truth sources, which are ranging between 1 and 3.

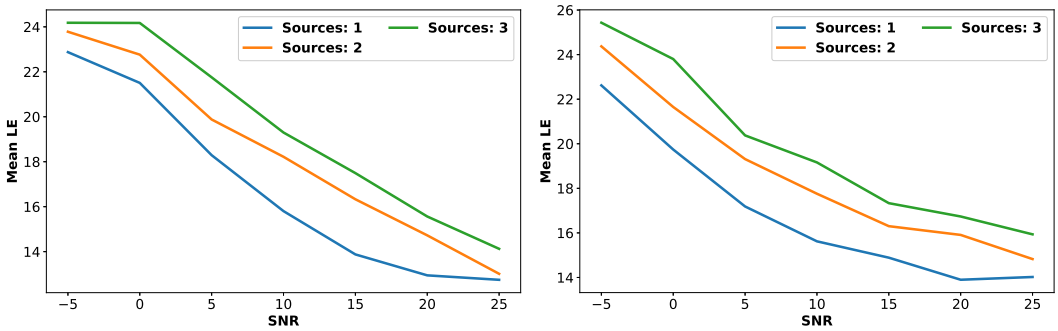

(A) CNN (B) ResNet18

FIGURE 6.4: Mean localization error for different number of ground-truth sources

From Figure 6.4, we can observe that the localization error increases in both ResNet18 and CNN as the number of ground-truth sources increases. Moreover, our custom CNN outperfomrs random in both higher and lower SNR values and for all numbers of ground-truth sources.

Now, we are analyzing the percentage of found sources for various SNR levels and numbers of ground-truth sources, ranging from 2 to 3. Figure 6.5 shows that our custom CNN can localize more sources across all SNR levels and numbers of ground-truth sources.

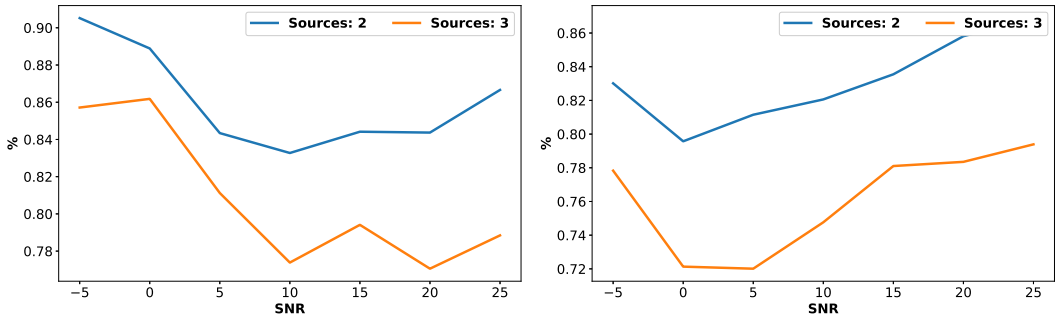

(A) CNN (B) ResNet18

FIGURE 6.5: Percentage of found sources for different number of ground-truth sources

6.3 Qualitative results

6.4 Simulated results summary

Our custom CNN consistently outperforms all ResNet [10] models and the traditional non Deep Learning technique sLORETA [25]. This finding demonstrates the robustness and effectiveness of our simulation (Chapter 5.3) and training (Chapter 5.5.3) procedures. Our model is also able to generalize and provide high-quality EEG localizations for multiple sources and different SNR levels. Since our custom CNN yielded the best performance we will continue our analysis with it.

6.5 Evaluation with Real data

Following feCNN [5], we will evaluate on real EEG recordings that contain data with one source activation from three different anatomies. Briefly, we will describe the data acquisition and the expected localization.

6.5.1 Data Acquisition

The real EEG data were recorded during the PhD [7] of Dr. Antonakakis and specifically are from this paper [97]. The EEG recordings of one of the participants in the study can be found here [98].

As described in [97], five *right-handed* subjects (three of them were 27 one 32 and the last 49 years old; 2 females) participated in the study. Somatosensory evoked potentials (SEP) and fields (SEF) were simultaneously acquire in a magnetically shielded room using 80 AgCl sintered ring electrodes (EASYCAP GmbH, Herrsching, Germany, 74 EEG channels plus additional six channels to detect eye movements).

For the detection of cardiac activity, electrocardiography (ECG) was additionally measured. Prior to the measurements, the electrode positions of the EEG cap were digitized using a Polhemus device (FASTRAK, Polhemus Incorporated, Colchester, VT).

A MAGNETOM Prisma 3.0 T (Release D13, Siemens Medical Solutions, Erlangen, Germany) was used for the acquisition of MRI datasets. A 3D-T1-weighted (T1w) was measured with fast gradient-echo pulse sequence (TFE) using water selective excitation to avoid fat shift (TR/TE/FW = 2300/3.51 ms/8°, inversion prepulse with TI =1.1 s, cubic voxels of 1 mm edge length); 3D-T2w turbo spin-echo pulse sequence (TR/TE/FA = 3200/408 ms/90°, cubic voxels, 1 mm edge length) and DTI using an echo-planar imaging sequence (TR/TE/FA = 9500/79 ms/90°, cubic voxels, 1.89 mm edge length), with one volume with diffusion sensitivity b = 0s / mm^2 (i.e., flat diffusion gradient) and 20 volumes with b = 1,000s / mm^2 in different directions, equally distributed on a sphere.

An additional volume with flat diffusion gradient, but with reversed spatial encoding gradients was scanned and utilized for susceptibility artifact correction. During T1w-MRI measurement, gadolinium markers were placed at the same nasion, left and right distal outer ear canal positions for landmark-based registration of EEG to MRI.

6.5.2 Stimulation

The somatosensory stimulation was conducted with the following experiment [97]. The median nerve at the *right wrist* was stimulated with monophasic square-wave electrical pulses having a duration of 0.5 ms. The stimulus strength was increased until a clear movement of the thumb was visible. This type of stimulation is abbreviated as EW stimulation.

The data were acquired with a sampling rate of 1,200 Hz and online filtered with a 300 Hz low pass filter. The experiment consisted of 1,200 trials. The stimulus onset asynchrony (SOA) varied randomly from 350-450 ms to avoid habituation and to allow obtaining clear prestimulus intervals for signal-to-noise ratio (SNR) determination.

6.5.3 Expected Localization

In actual EEG recordings, as opposed to simulations, we are unable to determine the precise location of the cluster of dipoles responsible for generating the observed electrical activity. Since we lack a definitive reference point for the true sources of EEG signals in real-world scenarios, we cannot rely on localization error as a measure to assess the performance of Inverse Methods. However, as described in Section 6.5.1, the EEG-recordings were generated by a very specific experiments with particular parameters, thus, we can know the approximate location of the seed dipole.

In the study [99] participated five *right-handed* male volunteers ages 21 to 36. The participants were stimulated with an air-puff-derived tactile stimulator which provides a light, superficial pressure stimulus to the skin surface. About 40 points in the right hemibody (including the tongue, lips, hand, arm, trunk, leg, and foot) were stimulated in a randomly determined order (see Figure 6.6).

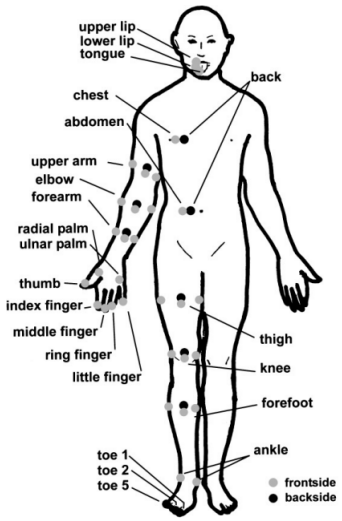

FIGURE 6.6: Forty-three stimulated points of the right hemibody. Adapted from [99]

Having collected EEG recordings for each stimulation and then employed source analysis techniques. This analysis involved modeling a single moving equivalent current dipole (ECD) within a spherical volume conduction. For each stimulation, we estimated the ECD's best-fitting location in terms of its x, y, and z coordinates, its orientation, and its dipole momention.

In general, when examining ECDs following chest stimulation, they were consistently found to be situated in the left postcentral gyrus. Regarding tongue stimulation, the ECD was positioned at the most inferior point, followed by the lips, fingers, and arm. Interestingly, there was a gradual shift in their locations towards superior and medial positions along the central sulcus, as illustrated in Figure 6.7.

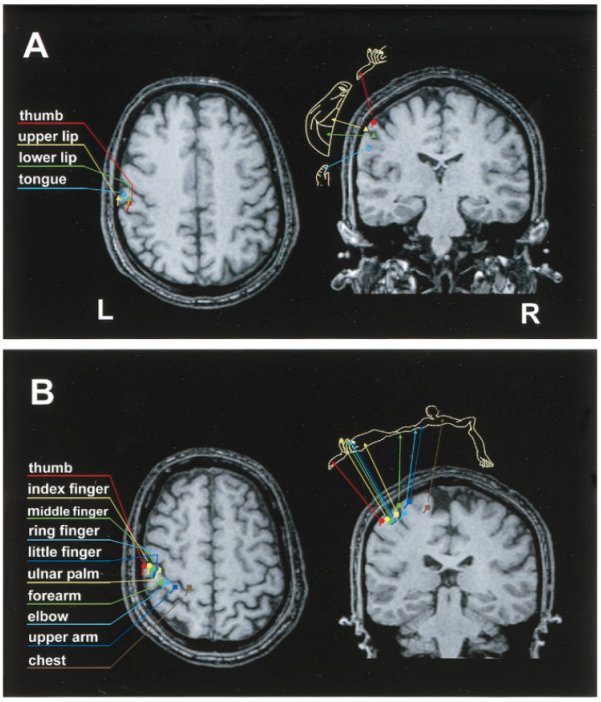

FIGURE 6.7: Expected localization of each stimulus. Adapted from [99]

Taking a closer look, research has uncovered the cytoarchitectonic subdivisions within the primary sensory cortex (S1). Specifically, these subdivisions include areas 3a, 3b, 1, and 2, which define the boundaries of the cortex within the postcentral gyrus, as illustrated in Figure 6.8.

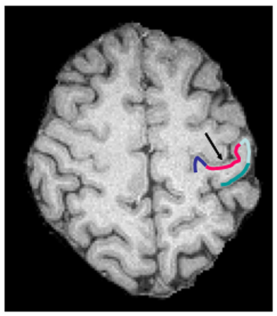

FIGURE 6.8: Areas of S1 as defined in cytoarchitectonic studies. Adapted from [100]

Figure 6.8 provides a visual representation of the cytoarchitectonic divisions within the primary sensory cortex. In this figure, you can observe that area 3a is situated at the bottom of the central sulcus, indicated by a dark blue shading. Area 3b occupies the front portion of the postcentral gyrus, marked in red. The crown of the postcentral gyrus, depicted in light blue, corresponds to area 1, while the posterior wall, shown in green, represents area 2. To aid in orientation, the black arrow points to the central sulcus.

Figure 6.9 displays the activation observed in the somatosensory cortex of the opposite hemisphere when the fingers of the right hand are subjected to tactile stimulation. The initial column presents transverse anatomical images with the z-coordinate provided for reference. In the following columns, you can see the activation patterns within the primary sensory cortex (S1) superimposed on magnified T1-weighted images, each corresponding to a different finger. The precise location of the highest activity voxel in area 3b is marked by blue crosshairs.

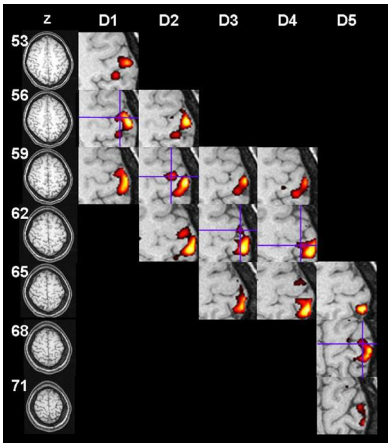

FIGURE 6.9: Activation on the S1. Adapted from [100]

These two experiments[99, 100] are pertinent to ours because:

- Participants in both studies fall within a similar age range.
- Both studies involve right-handed participants.

- It's worth noting that the stimulus applied to the right wrist is inherently incorporated in both studies [99] and [100]. This is because stimulating the right wrist results in the activation of both the thumb and the index finger.

Additionally, the findings in both [99] and [100] carry a high degree of reliability, stemming from their validation across numerous subjects and diverse brain anatomies. Consequently, we can consider the resulting localization data as reliable references.

In summary, when we synthesize the insights from both research studies [99, 100], it becomes evident that stimulating the right wrist in a right-handed individual elicits electrical activation within the primary sensory cortex (S1). Notably, this activation predominantly occurs in area 3b, which corresponds to the anterior wall of the postcentral gyrus (as indicated by the red shading in Figure 6.8). In the following section, we will demonstrate that our Convolutional Neural Network (CNN) successfully localizes this type of EEG recording to the anticipated location.

6.5.4 Results

To assess the effectiveness of our Convolutional Neural Network (CNN) and other inverse algorithms under realistic conditions, we employed actual EEG data that was acquired in accordance with the procedures outlined in Section 6.5.1. Utilizing the preprocessed and noise-free EEG signals, we conducted a performance evaluation by comparing our neural network with the conventional numerical technique sLORETA [25] and the recently introduced feCNN [5]. For the evaluation, we applied our CNN to EEG data collected from three of the five participants previously studied in [97].

The *first subject* is a 49 years old male. The recorded EEG signal and the produced topography (which is the input of our CNN) are shown in the Figure 6.10

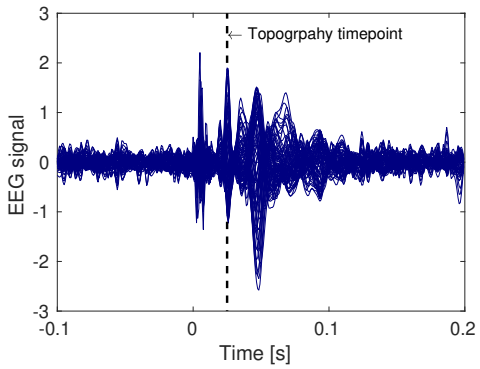

(A) EEG Signal

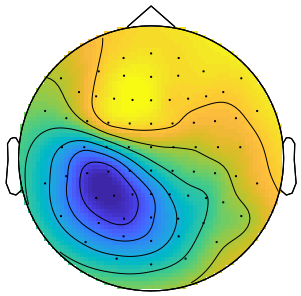

(B) Topography

FIGURE 6.10: Recorded data from subject 1

In the left plot, you'll notice a vertical black dotted line that signifies the specific timepoint at which the topographical representation was generated. During this timepoint, the conventional algorithms take the measurements from all 74 EEG-electrodes as their input, whereas our CNN and feCNN utilize the topography as their input.

We now present the source localization for the first subject:

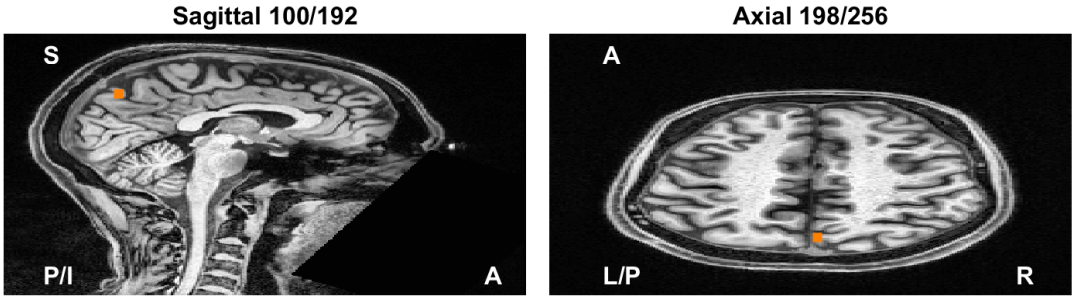

(A) Our CNN

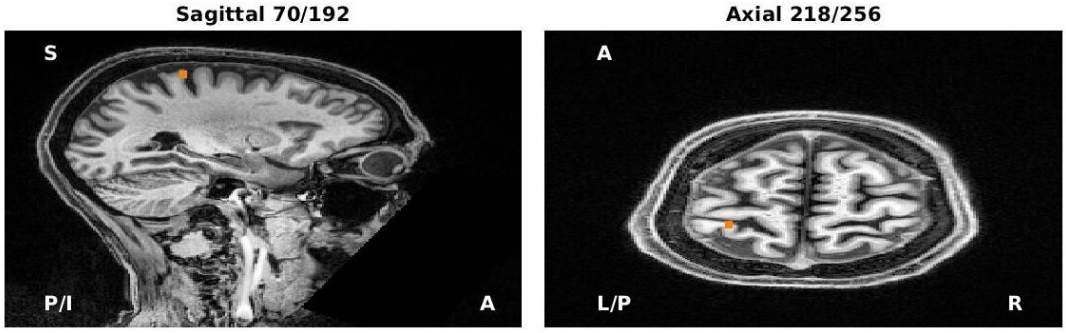

(B) feCNN [5]

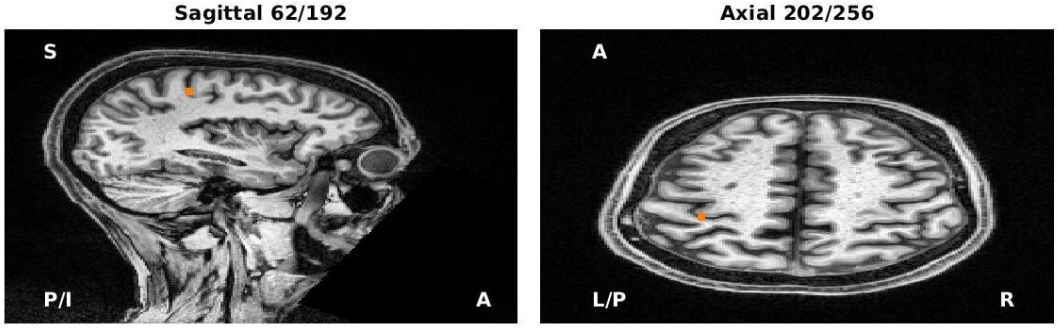

(C) sLORETA [25]

FIGURE 6.11: Source Localization for subject 1

The *second subject* is a 27 years old female. The recorded EEG signal and the produced topography (which is the input of our CNN) are shown in the Figure 6.12

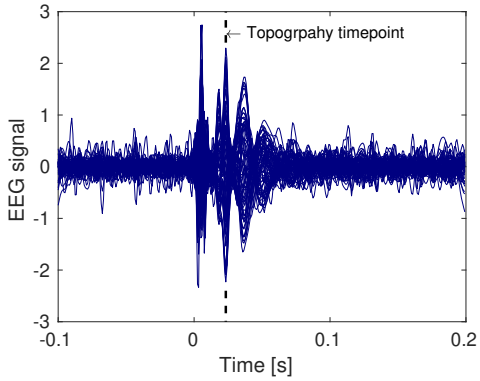

(A) EEG Signal

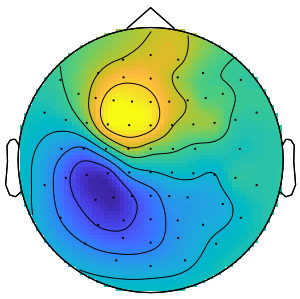

(B) Topography

FIGURE 6.12: Recorded data from subject 2

The source localization on the MRI of each method is shown in the Figure 6.13.

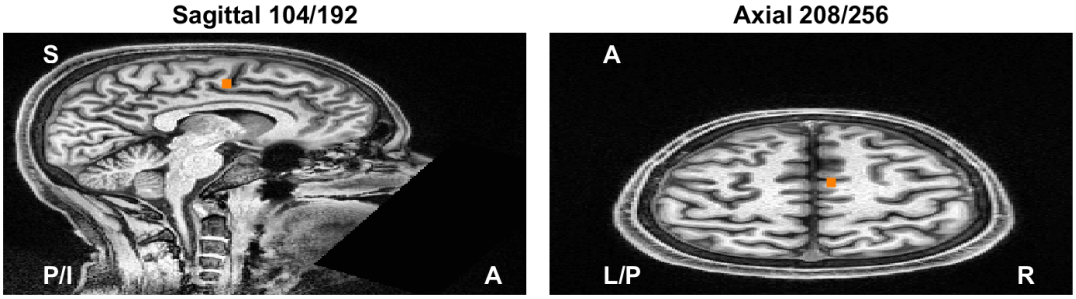

(A) Our CNN

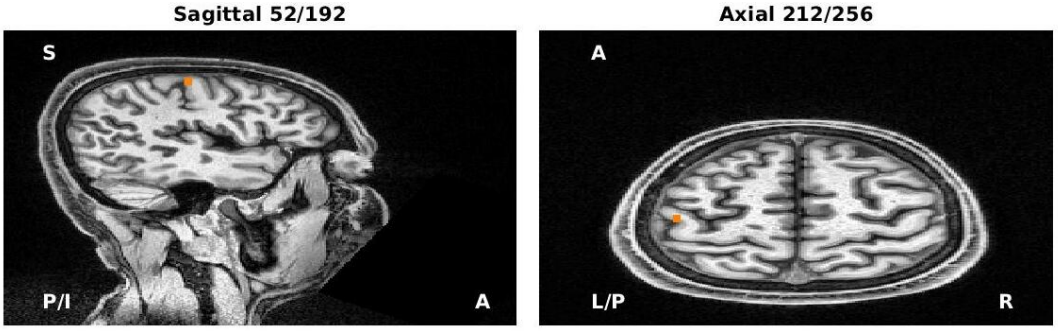

(B) feCNN [5]

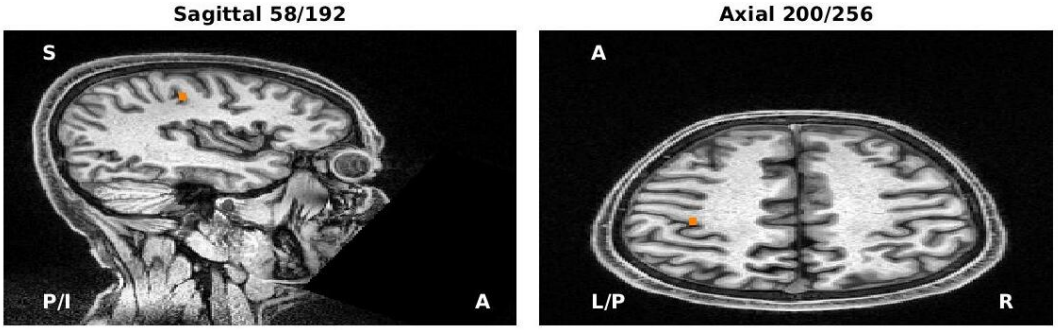

(C) sLORETA [25]

FIGURE 6.13: Source Localization for subject 2

The *third subject* is a 27 years old male. The recorded EEG signal and the produced topography (which is the input of our CNN) are shown in the Figure 6.14

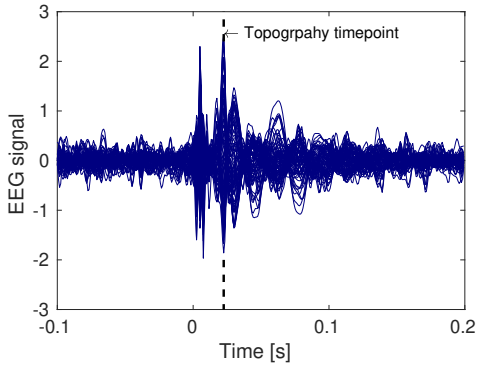

(A) EEG Signal

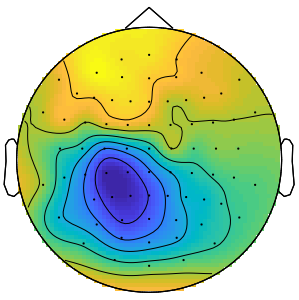

(B) Topography

FIGURE 6.14: Recorded data from subject 3

The source localization on the MRI of each method is shown in the Figure 6.15.

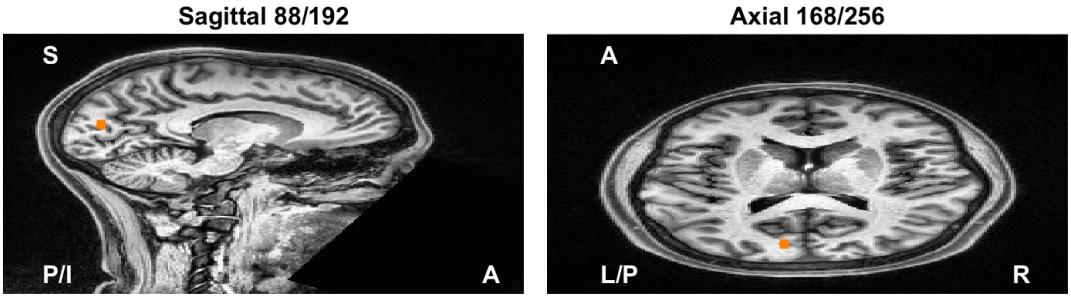

(A) Our CNN

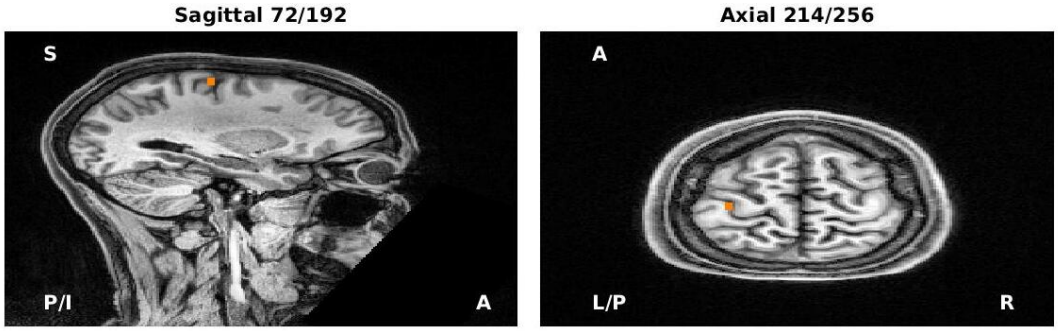

(B) feCNN [5]

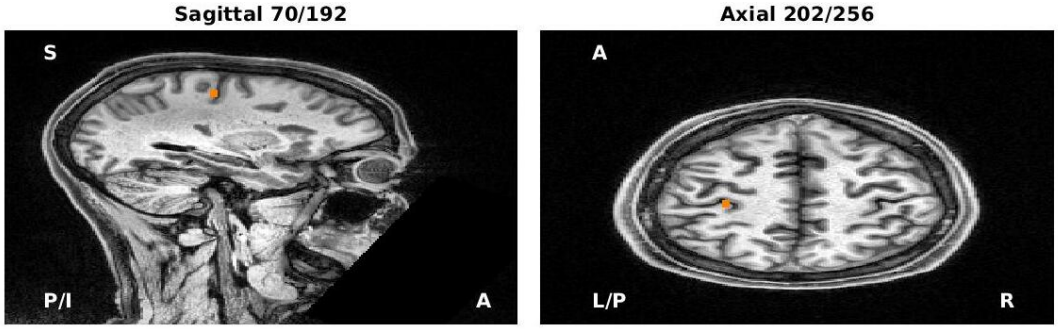

(C) sLORETA [25]

FIGURE 6.15: Source Localization for subject 3

As it can be seen from Figures 6.11,6.13,6.15, both feCNN [5] and sLORETA [25] generate the expected localization (see Section 6.5.3) ,for all the participants, which is the primary sensory cortex (S1). The localization of our model is close to primary sensory cortex and it is the only algorithm (among these two) to correctly localize more than one sources. In particular feCNN assumes only single source electrical activations while sLORETA generates very poor localizations for more than one sources.

Chapter 7

Conclusions

7.1 Summary

In this work we presented a model which solves the inverse problem of Source Analysis. Briefly, Source Analysis consists of two problems: the Forward and the Inverse problem. In the Forward problem we want to calculate the EEG signal given the electrical activation in the brain while in the Inverse we want to calculate the electrical activation given the EEG signal. The Forward problem is unrealistic as we cannot know the electrical activation in the brain while the Inverse has a wide range of applications including diagnosis of various diseases.

Since the Froward problem is unrealistic we simulate a dataset to train a neural network. The training dataset contains data from three brain-anatomies with up to three sources in the brain. For each data sample we first simualate the electrical activation in the brain (Chapter 5.3) and then calculate the EEG signal using Equation 5.2. We train our model to predict the electrical activation in the brain using as input a topography, which is generated from the EEG signal with Fieldtrip [92], with the MSE loss between the predicted and the simulated electrical activation.

Our mehtod, within the limited scope of our experiments, seems to compare favorably (Chapter 6) in comparison with the traditional sLORETA [25] approach for various SNR levels. Our findings can be summurized as follows:

- Our model outperforms sLORETA [25] for all SNR levels and all number of sources in simulated data.
- Our model can correctly localize EEG signals with very high noise levels ($<$ 0dB)
- The performance of our model depends on the number of sources.
- Our method generalizes on the real EEG data.
- We experimented with a ResNet [10] and a custom architecture and we observe that our custom model outperforms the ResNet.

7.2 Drawbacks and Future Directions

While our approach offers several advantages, it's important to acknowledge its drawbacks. Firstly, the orientation of dipoles within the head model must be constrained, as unrestricted orientation can significantly impact the results of source imaging. Our method does not estimate dipole orientations since the simulated EEG data lacks this information. Consequently, our model does not incorporate orientation information.

Additionally, our approach operates under the assumption of consistent smoothness in brain activity. Specifically, we generate synthetic source data that conforms to a Gaussian distribution. As a result, during the training process, our Convolutional Neural Network (CNN) learns to associate brain activity with smoothness and a Gaussian distribution.

Based on the drawbacks of our approach, there are still many directions worth exploring:

- **Dipole Orientations**: As previously mentioned, our model does not provide an estimate for the orientation of the reconstructed source. Therefore, it is worthwhile to explore an architecture capable of predicting the orientation of the source cluster.
- **Distribution of brain activity**:In our research, we generate synthetic source data that conforms to a Gaussian distribution. However, in reality, this assumption may not hold true. Therefore, we simulate brain activity samples, with a portion adhering to a Gaussian distribution, while the remainder follows a Random Markov Field distribution.
- **Inter-subject variability**: An advantage of the numerical methods is that they take into account the inter-subject variability of skull conductivity which causes the most significant influence on the EEG localization [101]. Therefore, it is worth investigating a new deep learning approach that can overcome the problem of the inter-subject variability.

Bibliography

[1] S.J. Luck. *An Introduction to the Event-Related Potential Technique*. MIT Press, 2014.

[2] Robert C Knowlton et al. "Functional imaging: I. Interictal and ictal SPECT". In: *Neurology* $66.12_{s}uppl_{3}$ (2006), S33–S44.

[3] Lukas Hecker and et al. "ConvDip: A Convolutional Neural Network for Better EEG Source Imaging". In: *Frontiers in Neuroscience* 15 (2021). DOI: 10.3389/fnins.2021.569918.

[4] Dimitrios Pantazis and Amir Adler. *MEG Source Localization via Deep Learning*. 2020. arXiv: 2012.00588 [eess.SP].

[5] Athanasios Delatolas et al. "EEG Source Analysis with a Finite-Element-based Convolutional Neural Network-feCNN". In: ().

[6] Chen Wei et al. "Edge sparse basis network: a deep learning framework for EEG source localization". In: *2021 International Joint Conference on Neural Networks (IJCNN)*. 2021, pp. 1–8.

[7] Marios Antonakakis. "The effect of experimental and modeling parameters on combined EEG/MEG source analysis and transcranial electric stimulation optimization of somatosensory and epilepsy activity". PhD thesis. 2021. URL: https://www.db-thueringen.de/receive/dbt_mods_00049153.

[8] Alex Krizhevsky, Ilya Sutskever, and Geoffrey E. Hinton. "ImageNet Classification with Deep Convolutional Neural Networks". In: *Advances in Neural Information Processing Systems (NeurIPS)* 25 (2012).

[9] Karen Simonyan and Andrew Zisserman. "Very Deep Convolutional Networks for Large-Scale Image Recognition". In: *International Conference on Learning Representations*. 2015.

[10] Kaiming He et al. "Deep residual learning for image recognition". In: *CVPR*. 2016.

[11] Gert Van Hoey et al. "EEG dipole source localization using artificial neural networks." In: *Physics in medicine and biology* 45 4 (2000), pp. 997–1011.

[12] Sung Chan Jun, Barak A Pearlmutter, and Guido Nolte. "Fast accurate MEG source localization using a multilayer perceptron trained with real brain noise". In: *Physics in Medicine & Biology* 47.14 (2002), p. 2547.

[13] Sung Chan Jun and Barak A Pearlmutter. "Fast robust subject-independent magnetoencephalographic source localization using an artificial neural network". In: *Human brain mapping* 24.1 (2005), pp. 21–34.

[14] Alexandra Razorenova et al. "Deep Learning for Non-invasive Cortical Potential Imaging". In: Dec. 2020, pp. 45–55. ISBN: 978-3-030-66842-6. DOI: 10.1007/978-3-030-66843-3_5.

[15] Rui Sun et al. "SIFNet: Electromagnetic Source Imaging Framework Using Deep Neural Networks". In: *bioRxiv* (2020). DOI: 10.1101/2020.05.11.089185. eprint: https://www.biorxiv.org/content/early/2020/07/09/2020.05.11.089185.full.pdf. URL: https://www.biorxiv.org/content/early/2020/07/09/2020.05.11.089185.

[16] Carsten Wolters et al. "Geometry-Adapted Hexahedral Meshes Improve Accuracy of Finite-Element-Method-Based EEG Source Analysis". In: *IEEE transactions on bio-medical engineering* 54 (Aug. 2007), pp. 1446–53. DOI: 10.1109/TBME.2007.890736.

[17] Mark W Woolrich et al. "Bayesian analysis of neuroimaging data in FSL". en. In: *Neuroimage* 45.1 Suppl (Nov. 2008), S173–86.

[18] Stephen M Smith et al. "Advances in functional and structural MR image analysis and implementation as FSL". en. In: *Neuroimage* 23 Suppl 1 (2004), S208–19.

[19] Mark Jenkinson et al. "FSL". en. In: *Neuroimage* 62.2 (Sept. 2011), pp. 782–790.

[20] Roberta Grech et al. "Review on solving the inverse problem in EEG source analysis". In: *Journal of NeuroEngineering and Rehabilitation* 5.1 (2008), p. 25. ISSN: 1743-0003. DOI: 10.1186/1743-0003-5-25. URL: https://doi.org/10.1186/1743-0003-5-25.

[21] David Wipf and Srikantan Nagarajan. "A unified Bayesian framework for MEG/EEG source imaging". eng. In: *NeuroImage* 44.3 (2009). 18602278[pmid], pp. 947–966. ISSN: 1095-9572. DOI: 10.1016/j.neuroimage.2008.02.059. URL: https://pubmed.ncbi.nlm.nih.gov/18602278.

[22] Matti S Hämäläinen and Risto J Ilmoniemi. "Interpreting magnetic fields of the brain: minimum-norm estimates". In: *Medical & biological engineering & computing* 32.1 (1994), pp. 35–42. DOI: 10.1007/BF02512476.

[23] Matti Hämäläinen et al. "Magnetoencephalography—theory, instrumentation, and applications to noninvasive studies of the working human brain". In: *Rev. Mod. Phys.* 65 (2 1993), pp. 413–497. DOI: 10.1103/RevModPhys.65.413. URL: https://link.aps.org/doi/10.1103/RevModPhys.65.413.

[24] R D Pascual-Marqui, C M Michel, and D Lehmann. "Low resolution electromagnetic tomography: a new method for localizing electrical activity in the brain". en. In: *Int J Psychophysiol* 18.1 (Oct. 1994), pp. 49–65.

[25] R.D. Pascual-Marqui. "Standardized low resolution brain electromagnetic tomography (SLORETA): Technical details". In: *Methods and findings in experimental and clinical pharmacology* 24 Suppl D (Feb. 2002), pp. 5–12.

[26] Munsif Ali Jatoi et al. "EEG based brain source localization comparison of sLORETA and eLORETA". en. In: *Australas Phys Eng Sci Med* 37.4 (Oct. 2014), pp. 713–721.

[27] Shiva Asadzadeh et al. "A systematic review of EEG source localization techniques and their applications on diagnosis of brain abnormalities". In: *Journal of neuroscience methods* 339 (2020), p. 108740.

[28] MUNSIF ALI JATOI. *Brain source localization using EEG signal analysis*. CRC Press, 2019.

[29] Garrett G. Gross et al. "Recombinant Probes for Visualizing Endogenous Synaptic Proteins in Living Neurons". In: *Neuron* 78.6 (2013), pp. 971–985. ISSN: 0896-6273. DOI: https://doi.org/10.1016/j.neuron.2013.04.017. URL: https://www.sciencedirect.com/science/article/pii/S089662731300319X.

[30] M McBride. *Pons*. SAGE Publications, Inc., 2004.

[31] Richard S Snell. *Clinical Neuroanatomy*. LWW, 2018.

[32] Patrice G Guyenet and Douglas A Bayliss. "Control of breathing and autonomic output by pontomedullary networks". In: *Respiratory physiology & neurobiology* 143.1 (2006), pp. 115–121.

[33] Clifford B Saper. *Sleep and the brain*. Elsevier, 2010.

[34] Eric R Kandel et al. *Principles of neural science*. McGraw-Hill Medical, 2012.

[35] Matthew Burns. "A Study of the Pons". In: *Journal of the Pontine Sciences* 4.2 (2012), pp. 27–34.

[36] Neil R Carlson. *Neuroscience*. Sinauer Associates, Inc., 2014.

[37] Eric R Kandel et al. *Principles of Neural Science*. McGraw-Hill Education, 2013.

[38] Alan R Crossman and David Neary. *Neuroanatomy: an illustrated colour text*. Elsevier Health Sciences, 2013.

[39] Steven J Luck. *An Introduction to the Event-Related Potential Technique*. MIT Press, 2005.

[40] Michal Teplan. "Fundamentals of EEG measurements". In: *Measurement Neuroscience Reviews* 2.2 (2002), pp. 1–11.

[41] J. H. Margerison, C. D. Binnie, and I. R. McCaul. "Electroencephalographic signs employed in the location of ruptured intracranial arterial aneurysms". In: *Electroencephalography and Clinical Neurophysiology* 28 (1970), pp. 296–306.

[42] H. H. Jasper. "The ten twenty electrode system of the international federation". In: *Electroencephalography and Clinical Neurophysiology* 10 (1958), pp. 371–375.

[43] H. Jasper. "Report of committee on methods of clinical exam in EEG". In: *Electroencephalography and Clinical Neurophysiology* 10 (1958), pp. 370–375.

[44] Gustave H. Klem et al. "The ten-twenty electrode system of the International Federation". In: *Electroencephalography and Clinical Neurophysiology* 52.3 (1999), pp. 3–6.

[45] Saeid Sanei and Jonathon A. Chambers. *EEG Signal Processing*. Hoboken, NJ: John Wiley & Sons, 2013.

[46] *Effects of electrode placement*. Available online. Accessed on January 16, 2017. URL: http://www.focused-technology.com/electrod.htm.

[47] Thomas Collura. *A Guide to Electrode Selection, Location, and Application for EEG Biofeedback*. Bedford, OH: Brain-Master Technologies, Inc., 1998.

[48] Roberto D Pascual-Marqui. "Standardized low-resolution brain electromagnetic tomography (sLORETA): technical details". In: *Methods and findings in experimental and clinical pharmacology* 24 (2002), pp. 5–12.

[49] Matti Hämäläinen and Risto J Ilmoniemi. "Interpreting magnetic fields of the brain: minimum norm estimates". In: *Medical & biological engineering & computing* 31.4$_s$*uppl* (1993), S35–S42.

[50] Claudio Babiloni et al. “EEG markers of cognitive decline in healthy subjects”. In: *Frontiers in human neuroscience* 3 (2009), p. 37.

[51] Anders M Dale and Eric Halgren. “Improved localization of cortical activity by combining EEG and MEG with MRI cortical surface reconstruction: a linear approach”. In: *Journal of cognitive neuroscience* 5.2 (1993), pp. 162–176.

[52] Kai J Miller, Roland Nigbur, and Miriam M Müller. “How to connect findings from neuroimaging and electrophysiology”. In: *Brain topography* 25.3 (2012), pp. 269–274.

[53] Andre M Bastos et al. “Canonical microcircuits for predictive coding”. In: *Neuron* 76.4 (2012), pp. 695–711.

[54] A. Taflove and S. C. Hagness. *Computational Electrodynamics*. Norwood, MA: Artech House, 2005.

[55] K. Yee. “Numerical solution of initial boundary value problems involving Maxwell’s equations in isotropic media”. In: *IEEE Transactions on Antennas and Propagation* 14 (1966), pp. 302–307.

[56] T. Weiland. “A discretization model for the solution of Maxwell’s equations for six-component fields”. In: *Archiv Elektronik und Uebertragungstechnik* 31 (1977), pp. 116–120.

[57] C. T. A. Johnk. *Engineering Electromagnetic Fields and Waves*. Vol. 667. New York: John Wiley & Sons, 1975, p. 1.

[58] H. A. Haus and J. R. Melcher. *Electromagnetic Fields and Energy*. Upper Saddle River, NJ: Prentice Hall, 1989.

[59] W. C. Chew. *Waves and Fields in Inhomogeneous Media*. Vol. 522. New York: IEEE Press, 1995.

[60] G. T. Markov and A. F. Chaplin. *The Excitation of Electromagnetic Waves*. Moscow, Russia: Moscow Izdatel Radio Sviaz, 1983.

[61] C. Ramon et al. “Role of soft bone, CSF and gray matter in EEG simulations”. In: *Brain Topography* 16 (2004), pp. 245–248.

[62] G. Pruis, B. H. Gilding, and M. Peters. “A comparison of different numerical methods for solving the forward problem in EEG and MEG”. In: *Physiological Measurement* 14 (1993), A1.

[63] K. A. Awada and et al. “Effect of conductivity uncertainties and modeling errors on EEG source localization using a 2-D model”. In: *IEEE Transactions on Biomedical Engineering* 45 (1998), pp. 1135–1145.

[64] K. A. Awada and et al. “Closed-form evaluation of flux integrals appearing in a FEM solution of the 2D Poisson equation with dipole sources”. In: *Electromagnetics* 16 (1996), pp. 75–90.

[65] Hans Hallez and et al. “Review on solving the forward problem in EEG source analysis”. In: *Journal of neuroengineering and rehabilitation* 4.1 (2007).

[66] Scott Rush and D. A. Driscoll. “Current distribution in the brain from surface electrodes”. In: *Anesthetics and Analgesia* 47 (1968), pp. 717–723.

[67] Sylvain Baillet. “Forward and Inverse Problems of MEG/EEG”. In: Jan. 2014, pp. 1–8. ISBN: 978-1-4614-7320-6. DOI: 10.1007/978-1-4614-7320-6_529-1.

[68] Carlos Alberto Brebbia. *Boundary element methods in engineering science*. Springer, 1984.

[69] Robert Grech et al. "Review on solving the forward problem in EEG source analysis". In: *Journal of neuroengineering and rehabilitation* 5.1 (2008), p. 25.

[70] John C Mosher, Peter S Lewis, and Richard M Leahy. "EEG and MEG: forward solutions for inverse methods". In: *IEEE Transactions on Biomedical Engineering* 39.9 (1992), pp. 963–969.

[71] Alan S Gevins and Martin E Cutillo. "Event-related brain potentials in man". In: *Annals of the New York Academy of Sciences* 425.1 (1987), pp. 56–73.

[72] Alexandre Gramfort et al. "MEG and EEG data analysis with MNE-Python". In: *Frontiers in neuroscience* 7 (2013), p. 267.

[73] Michael Scherg and Daniel E Berg. "Fundamentals of dipole source potential analysis". In: *Advances in audiology* 6 (1990), pp. 40–69.

[74] Thomas J.R. Hughes. *The Finite Element Method: Linear Static and Dynamic Finite Element Analysis*. Dover Publications, 1987.

[75] Christian Fuchs and Guido Nolte. "EEG and MEG: Forward solutions for inverse methods". In: *Brain Mapping: An Encyclopedic Reference*. Vol. 3. Academic Press, 2015, pp. 37–41.

[76] Jan C. De Munck. "The estimation of time varying dipoles on the basis of evoked potentials". In: *Electroencephalography and Clinical Neurophysiology* 77 (1990), pp. 156–160.

[77] Alberto Rodríguez-Rivera, Barry D Van Veen, and Ronald T Wakai. "Statistical performance analysis of signal variance-based dipole models for MEG/EEG source localization and detection". In: *IEEE Trans. Biomed. Eng.* 50.2 (Feb. 2003), pp. 137–149.

[78] DM Schmidt, JS George, and CC Wood. *Bayesian Inference Applied to the Electromagnetic Inverse Problem. Progress Report 1997–1998, Physics Division*. Tech. rep. Physics Division, 2002.

[79] Yann LeCun, Yoshua Bengio, and Geoffrey Hinton. "Deep learning". In: *Nature* 521.7553 (2015), pp. 436–444.

[80] Yoshua Bengio. "Learning deep architectures for AI". In: *Foundations and Trends® in Machine Learning* 2.1 (2009), pp. 1–127.

[81] Ian Goodfellow, Yoshua Bengio, and Aaron Courville. *Deep learning*. MIT Press, 2016.

[82] David E. Rumelhart, Geoffrey E. Hinton, and Ronald J. Williams. "Learning representations by back-propagating errors". In: *Nature* 323.6088 (1986), pp. 533–536.

[83] Yann LeCun, Yoshua Bengio, and Geoffrey Hinton. "Convolutional networks for images, speech, and time series". In: *The handbook of brain theory and neural networks*. Vol. 3361. 10. MIT Press, 1998, pp. 1995–2009.

[84] Nitish Srivastava et al. "Dropout: A Simple Way to Prevent Neural Networks from Overfitting". In: *Journal of Machine Learning Research* 15.1 (2014), pp. 1929–1958.

[85] Carsten H. Wolters et al. "Geometry-adapted hexahedral meshes improve accuracy of finite-element-method-based EEG source analysis". In: *IEEE Transactions on Biomedical Engineering* 54.8 (2007), pp. 1446–1453.

[86] E. Cuartas Morales et al. "A Finite-Difference Solution for the EEG Forward Problem in Inhomogeneous Anisotropic Media". In: *Brain Topography* 32.2 (2019), pp. 229–239.

[87] Johannes Vorwerk et al. "A guideline for head volume conductor modeling in EEG and MEG". In: *NeuroImage* 100 (2014), pp. 590–607.

[88] Carsten H. Wolters et al. "Influence of tissue conductivity anisotropy on EEG/MEG field and return current computation in a realistic head model: A simulation and visualization study using high-resolution finite element modeling". In: *NeuroImage* 30.3 (2006), pp. 813–826.

[89] Sophie Schrader and et al. "DUNEuro—A software toolbox for forward modeling in bioelectromagnetism". In: *PLOS ONE* 16.6 (2021), pp. 1–21. DOI: 10.1371/journal.pone.0252431. URL: https://doi.org/10.1371/journal.pone.0252431.

[90] Carsten Wolters, Lars Grasedyck, and Wolfgang Hackbusch. "Efficient Computation of lead field bases and influence matrix for the FEM-based EEG and MEG inverse problem". In: *Inverse Problems* 20 (2004), pp. 1099–1116. DOI: 10.1088/0266-5611/20/4/007.

[91] Marios Antonakakis. "The effect of experimental and modeling parameters on combined EEG/MEG source analysis and transcranial electric stimulation optimization of somatosensory and epilepsy activity". PhD Thesis. 2021. URL: https://www.db-thueringen.de/receive/dbt_mods_00049153.

[92] Robert Oostenveld et al. "FieldTrip: Open Source Software for Advanced Analysis of MEG, EEG, and Invasive Electrophysiological Data". In: *Computational Intelligence and Neuroscience* 2011 (2011), p. 156869. DOI: 10.1155/2011/156869. URL: https://doi.org/10.1155/2011/156869.

[93] Aston Zhang et al. *Dive into Deep Learning*. Interactive online book, Chapter 8.5. 2021. URL: https://d2l.ai.

[94] Diederik P. Kingma and Jimmy Ba. "Adam: A Method for Stochastic Optimization". In: *ICLR*. 2017.

[95] François Tadel et al. "Brainstorm: A User-Friendly Application for MEG/EEG Analysis". In: *Computational Intelligence and Neuroscience* 2011 (2011), p. 879716. ISSN: 1687-5265. DOI: 10.1155/2011/879716. URL: https://doi.org/10.1155/2011/879716.

[96] Felix Lucka et al. "Hierarchical Bayesian inference for the EEG inverse problem using realistic FE head models: depth localization and source separation for focal primary currents". In: *NeuroImage* 61.4 (2012), pp. 1364–1382.

[97] Marios Antonakakis et al. "The effect of stimulation type, head modeling, and combined EEG and MEG on the source reconstruction of the somatosensory P20/N20 component". In: *Human Brain Mapping* 40.17 (2019), pp. 5011–5028. DOI: https://doi.org/10.1002/hbm.24754. eprint: https://onlinelibrary.wiley.com/doi/pdf/10.1002/hbm.24754. URL: https://onlinelibrary.wiley.com/doi/abs/10.1002/hbm.24754.

[98] Maria Carla Piastra et al. *The WWU DUNEuro reference data set for combined EEG/MEG source analysis*. The research related to this dataset was supported by the German Research Foundation (DFG) through project WO1425/7-1 and the EU project ChildBrain (Marie Curie Innovative Training Networks, grant agreement 641652). June 2020. DOI: 10.5281/zenodo.3888381. URL: https://doi.org/10.5281/zenodo.3888381.

[99] Akinori Nakamura et al. “Somatosensory Homunculus as Drawn by MEG”. In: *NeuroImage* 7.4 (1998), pp. 377–386. ISSN: 1053-8119. DOI: https://doi.org/10.1006/nimg.1998.0332. URL: https://www.sciencedirect.com/science/article/pii/S1053811998903329.

[100] Danielle van Westen et al. “Fingersomatotopy in area 3b: an fMRI-study”. en. In: *BMC Neurosci* 5 (Aug. 2004), p. 28.

[101] Marios Antonakakis et al. “Inter-Subject Variability of Skull Conductivity and Thickness in Calibrated Realistic Head Models”. en. In: *Neuroimage* 223 (Sept. 2020), p. 117353.